

Upper bounds on the separation efficiency of diffusiophoresis

Fernando Temprano-Coleto,^{†,‡} Jeongmin Kim,[†] Marcel M. Louis,[†] and Howard A. Stone^{*,†}

[†] Department of Mechanical and Aerospace Engineering, Princeton University, Princeton, NJ 08544, USA

[‡] Andlinger Center for Energy and the Environment, Princeton University, Princeton, NJ 08544, USA

E-mail: hastone@princeton.edu

Abstract

The separation of colloidal particles from fluids is essential to ensure a safe global supply of drinking water yet, in the case of microscopic particles, it remains a highly energy-intensive process when using traditional filtration methods. Water cleaning through diffusiophoresis—spontaneous colloid migration in chemical gradients—effectively circumvents the need for physical filters, representing a promising alternative. This separation process is typically realized in internal flows where a cross-channel electrolyte gradient drives particle accumulation at walls, with colloid separation slowly increasing in the streamwise direction. However, the maximum separation efficiency, achieved sufficiently downstream as diffusiophoretic migration (driving particle accumulation) is balanced by Brownian motion (inducing diffusive spreading), has not yet been characterized. In this work, we develop a theory to predict this upper bound, and derive the colloid separation efficiency by analyzing the asymptotic structure of the governing equations. We find that the mechanism by which the chemical permeates in the channel, as well as the reaction kinetics governing its dissociation into ions, play key roles in the process. Moreover, we identify four distinct regimes in which separation is controlled by different scaling laws involving a Damköhler and a Péclet number, which measure the ratio of reaction kinetics to ion diffusion and of diffusiophoresis to Brownian motion, respectively. We also confirm the scaling of one of these regimes using microfluidic experiments where separation is driven by CO_2 gradients. Our results shed light on pathways towards new, more efficient separations, and are also applicable to quantify colloidal accumulation in the presence of chemical gradients in more general situations.

Introduction

Colloidal suspensions spontaneously migrate in the presence of electrolyte gradients through a physicochemical mechanism known as diffusiophoresis. Since its discovery by Derjaguin^{1,2} and its subsequent theoretical formalization^{3–6}, many studies have used this phenomenon to manipulate particle motion at small scales. Applications include colloid focusing^{7–10}, custom particle migration^{11–13}, particle delivery into porous structures^{14–17}, or the characterization of colloidal properties^{18,19}, among others^{20,21}.

Diffusiophoresis has also been shown to induce the continuous removal of colloidal particles from water^{22–27}. In this scenario, separation is typically achieved by field-flow fractionation, where a flowing colloidal suspension is subject to a cross-channel chemical gradient. The resulting phoretic motion drives particles to accumulate near channel walls, creating particle-depleted regions near the channel center that can be diverted to obtain clean water. This chemically-driven process requires no electrical input beyond the power required for pumping, and circumvents the use of physical filters that become highly energy intensive for small particles since their membrane pore size

must also scale with the particle size^{28,29}. Therefore, diffusiophoresis has been highlighted as an energy-efficient alternative to traditional filtration, increasingly needed with the rise of emerging contaminants like microplastics and nanoplastics, now widespread in virtually every source of water^{30–32}.

Existing theories to predict diffusiophoresis-driven colloid separation have so far focused on how particle distributions evolve downstream after a chemical cross-channel gradient is established^{24,26}. However, the maximum degree of separation, which is achieved sufficiently downstream as the particle distributions become invariant in the streamwise direction, has not yet been explored. Quantifying such a regime, which yields a theoretical upper bound for how much clean water can be recovered from a particle suspension through diffusiophoresis alone, is necessary to assess the potential scalability and feasibility of this type of separation. In this study, we formulate a continuum theory for this regime, where the two dominant effects are the diffusiophoresis-induced advection of particles, driving particles to accumulate at channel walls, and the Brownian motion of the colloids, which diffusively smooths the colloid distribution and hinders separation.

The main conclusion of our analysis is that

separation depends strongly on the type of chemical source employed, distinguishing between a gas diffusing into the channel through a nonporous membrane and a liquid permeating through a porous membrane. Similarly, dissociation kinetics of the chemical into the ions driving the process also plays a key role, with different predictions depending on the rate of dissociation. Using asymptotic analysis, we provide scaling relations that predict separation in four distinct regimes, which are confirmed to be valid by numerical simulations. Finally, we provide experimental verification of one of these regimes by measuring colloid separation in microfluidic channels under a sustained gradient of carbon dioxide.

Theory

Problem setup

We consider an aqueous suspension of solid particles flowing in a two-dimensional channel at steady state (Figure 1), with X and Y the streamwise and spanwise coordinates, respectively. The wall at $Y = 0$ is a membrane that allows a solute \mathcal{S} to permeate into the channel from a source, and whose molar concentration we denote by $C_s(X, Y) := [\mathcal{S}]$. This solute dissociates in water through the reaction



with \mathcal{C} a cation, \mathcal{A} an anion, $\nu_{\mathcal{C}}$ and $\nu_{\mathcal{A}}$ the number of cation and anion moles produced by the dissociation of one mole of \mathcal{S} , and k_f and k_r the forward and reverse rate constants, respectively. We further assume that (1) is the dominant chemical equilibrium in the bulk liquid, thus regarding $[\mathcal{C}]$, $[\mathcal{A}]$ and $[\mathcal{S}]$ as much larger than the concentrations of any other species possibly arising from additional chemical reactions.

This assumption implies that we can consider the solution a *binary electrolyte*, in which case we can define a single “reduced” ionic concentration

$$C_i(X, Y) := \frac{[\mathcal{C}]}{\nu_{\mathcal{C}}} = \frac{[\mathcal{A}]}{\nu_{\mathcal{A}}}. \quad (2)$$

This simplification arises from the electroneutrality of the solution³³, which should only break down within distances of the order of the Debye-Hückel screening length λ_D of the (charged) channel walls. This length typically ranges between a few nanometers and a few microns, and is therefore much smaller than the width W of the channel in this work, i.e. $\lambda_D \ll W$. We also consider the reactions (1) to be elementary and the two species C_s and C_i to be sufficiently dilute to regard the electrolyte as an ideal solution. Accordingly, the reaction rates depend on concentration following the law of mass action, so we define $R := k_f[\mathcal{S}] - k_r[\mathcal{C}]^{\nu_{\mathcal{C}}}[\mathcal{A}]^{\nu_{\mathcal{A}}}$ as

an overall chemical reaction rate. Using (2), we obtain

$$R(C_s, C_i) = k_f C_s - k_r \nu_{\mathcal{C}}^{\nu_{\mathcal{C}}} \nu_{\mathcal{A}}^{\nu_{\mathcal{A}}} C_i^{\nu}, \quad (3)$$

where we have defined $\nu := \nu_{\mathcal{C}} + \nu_{\mathcal{A}}$. In the case of symmetric $z:z$ electrolytes, such as those arising from the dissociation of salts like NaCl³⁴ or gases like CO₂^{20,22,24,26,35,36}, we have $\nu_{\mathcal{C}} = \nu_{\mathcal{A}} = 1$ and $\nu = 2$. However, the value of ν can be higher for asymmetric electrolytes such as CaCl₂ ($\nu = 3$), Na₃PO₄ ($\nu = 4$), or Al₂(SO₄)₃ ($\nu = 5$), so we assume $\nu \geq 2$ in general.

The spatial distributions of C_s and C_i are therefore governed by two coupled partial differential equations:

$$U \frac{\partial C_s}{\partial X} = D_s \left(\frac{\partial^2 C_s}{\partial X^2} + \frac{\partial^2 C_s}{\partial Y^2} \right) - R(C_s, C_i), \quad (4a)$$

$$U \frac{\partial C_i}{\partial X} = D_i \left(\frac{\partial^2 C_i}{\partial X^2} + \frac{\partial^2 C_i}{\partial Y^2} \right) + R(C_s, C_i), \quad (4b)$$

where $U(Y)$ is the velocity field inside the channel, D_s is the diffusivity of the solute, and D_i is the ambipolar diffusivity³³ of the ions. The system of equations (4) gives rise to spatial gradients in the ionic concentration, which in turn induces a diffusiophoresis-driven migration velocity

$$\mathbf{U}_p = \Gamma_p \frac{\nabla C_i}{C_i} \quad (5)$$

of the particles in the suspension⁵. The constant Γ_p is the diffusiophoretic mobility, dependent on both the composition of the electrolyte and the properties of the particles, and which can be both positive (leading to “chemo-attracted” particles) or negative (resulting in “chemo-repelled” particles). Denoting the X and Y components of \mathbf{U}_p , respectively, as U_p and V_p , the concentration $N(X, Y)$ of particles is given by

$$\frac{\partial((U + U_p)N)}{\partial X} + \frac{\partial(V_p N)}{\partial Y} = D_p \left(\frac{\partial^2 N}{\partial X^2} + \frac{\partial^2 N}{\partial Y^2} \right), \quad (6)$$

where D_p is the diffusivity of the particles arising from their Brownian motion. After the chemical source is set in contact with the channel at $X = 0$ (Figure 1a), the solute, ions, and particles are first *developing*, with C_s , C_i , and N slowly changing in the streamwise direction X . This case, as well as its implications for the separation of colloids, has been studied previously by several authors^{22–24,26}.

In contrast, here we study the limit in which the system given by (4) and (6) reaches a *fully-developed* state (Figure 1b). Sufficiently far downstream, the fields C_s , C_i and N become invariant in the streamwise direction, i.e. $\partial_X C_s = \partial_X C_i = 0$, leading to

$$D_s \frac{d^2 C_s}{dY^2} = [k_f C_s - k_r \nu_{\mathcal{C}}^{\nu_{\mathcal{C}}} \nu_{\mathcal{A}}^{\nu_{\mathcal{A}}} C_i^{\nu}], \quad (7a)$$

$$D_i \frac{d^2 C_i}{dY^2} = -[k_f C_s - k_r \nu_{\mathcal{C}}^{\nu_{\mathcal{C}}} \nu_{\mathcal{A}}^{\nu_{\mathcal{A}}} C_i^{\nu}]. \quad (7b)$$

In this fully developed regime, chemical gradients are sustained through the continuous diffusion of solute into the channel from the chemical source at $Y = 0$, but also through its withdrawal into a chemical sink at $Y = W$ (see Figure 1b). Accordingly, we set

$$C_s = C_{s0} \quad \text{at } Y = 0, \text{ and} \quad (8a)$$

$$C_s = C_{s*} \quad \text{at } Y = W, \quad (8b)$$

as boundary conditions, where C_{s0} and C_{s*} are reference concentrations imposed by the chemical source and sink, respectively. Boundary conditions for the ionic species C_i depend on the mechanism of solute transport through the channel membrane walls. On one hand, for a *liquid* reservoir the solute itself permeates into the channel via fluid flow through the porous wall. This setup can be achieved, for instance, using hydrogel membranes in microfluidics^{8,34,37–39}. In this case, the solution composition at channel walls must match the concentrations of the source and sink, i.e.

$$C_i = C_{i0} \quad \text{at } Y = 0, \text{ and} \quad (9a)$$

$$C_i = C_{i*} \quad \text{at } Y = W. \quad (9b)$$

Here, C_{i0} and C_{i*} are the ionic concentrations set by C_{s0} and C_{s*} at chemical equilibrium. These values can be obtained imposing detailed balance in the reaction term $R(C_{s*}, C_{i*}) = R(C_{s0}, C_{i0}) = 0$, which yields

$$C_{i0} = \left(\frac{k_f C_{s0}}{k_r \nu_C^{\nu_C} \nu_A^{\nu_A}} \right)^{1/\nu}, \quad (10a)$$

$$C_{i*} = \left(\frac{k_f C_{s*}}{k_r \nu_C^{\nu_C} \nu_A^{\nu_A}} \right)^{1/\nu}. \quad (10b)$$

On the other hand, in *gas* sources the chemical permeates through the membrane by way of a

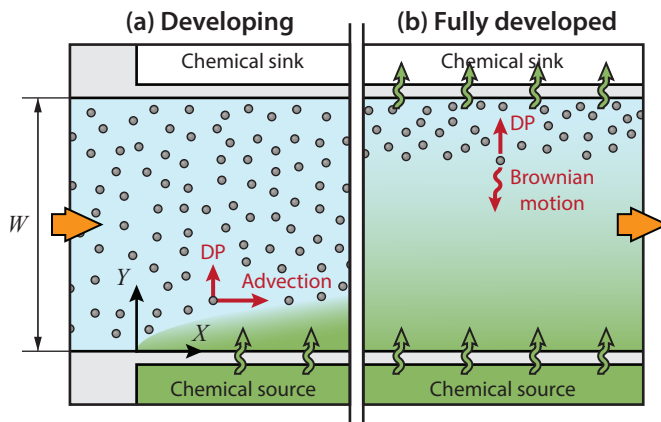


Figure 1: Colloid separation through diffusiophoresis in field-flow fractionation. (a) Upstream, the interplay between flow advection and the permeation of the chemical results in a *developing* distributions of chemical species and particles. (b) Sufficiently far downstream, all fields are *fully-developed* and invariant in the streamwise direction.

solution-diffusion mechanism⁴⁰, then dissolves in the aqueous solution to produce the solute, which in turn dissociates into the ions. This setup has been realized in microfluidics using CO_2 and gas-permeable polydimethylsiloxane (PDMS) devices^{22,24,26}. Since the walls are only gas-permeable, ions in solution cannot diffuse through them, such that

$$\frac{dC_i}{dY} = 0, \quad \text{at } Y = 0 \text{ and } Y = W. \quad (11)$$

Regarding the concentration of particles, in the fully developed regime we expect that $\partial_X N = 0$, leading to

$$\frac{d(V_p N)}{dY} = D_p \frac{d^2 N}{dY^2}, \quad (12)$$

which is supplemented by boundary conditions specifying a zero particle flux at channel walls,

$$V_p N - D_p \frac{dN}{dY} = 0, \quad \text{at } Y = 0 \text{ and } Y = W. \quad (13)$$

The particle concentration given by (12) and (13) is only defined up to a multiplicative constant, which can be fixed by imposing an average value N_0 given by

$$\frac{1}{W} \int_0^W N(Y) dY = N_0. \quad (14)$$

Nondimensionalization. We seek to understand how the problem parameters affect the spatial distribution of particles $N(Y)$, so we first define the nondimensional variables $y := Y/W$, $c_s := C_s/C_{s0}$, $c_i := C_i/C_{i0}$, and $n := N/N_0$. Following this normalization, the particle concentration follows an ordinary differential equation (ODE) given by

$$\pm Pe_p \frac{d}{dy} (v_p n_{\pm}) = \frac{d^2 n_{\pm}}{dy^2}, \quad (15)$$

where we define the particle Péclet number as

$$Pe_p := \frac{|\Gamma_p|}{D_p} > 0, \quad (16)$$

and where the signs distinguish between the case where the mobility is positive $\Gamma_p > 0$ and the particles $n_{+}(y)$ are chemo-attracted, from the case where $\Gamma_p < 0$ and the particles $n_{-}(y)$ are chemo-repelled. We have also defined a nondimensional particle migration velocity $v_p := V_p W/\Gamma_p$, related to $c_i(y)$ through

$$v_p = \frac{1}{c_i} \frac{dc_i}{dy}. \quad (17)$$

Equation (15), along with (17) and conditions

$$\pm Pe_p v_p n_{\pm} - \frac{\partial n_{\pm}}{\partial y} = 0 \quad \text{at } y = 0 \text{ and } y = 1, \quad (18a)$$

$$\int_0^1 n_{\pm}(y) dy = 1, \quad (18b)$$

which are the nondimensional equivalents of (13) and (14), respectively, can be integrated for an arbitrary ionic concentration $c_i(y)$. The solution is

$$n_{\pm}(y) = \frac{c_i(y)^{\pm Pe_p}}{\int_0^1 c_i(y)^{\pm Pe_p} dy}. \quad (19)$$

This power-law behavior of the particle distribution in Pe_p has also been recently reported in theories for colloid trapping in chemical gradients¹⁰. While Equation (19) is an exact result, the particles $n_{\pm}(y)$ still depend on the concentration $c_i(y)$, which is in turn given by the dimensionless versions of (7), namely

$$\frac{1}{Da_s} \frac{d^2 c_s}{dy^2} = [c_s - c_i^\nu], \quad (20a)$$

$$\frac{1}{Da_i} \frac{d^2 c_i}{dy^2} = -[c_s - c_i^\nu]. \quad (20b)$$

Here, we have defined two Damköhler numbers

$$Da_s := \frac{k_f W^2}{D_s}, \quad (21a)$$

$$Da_i := \frac{k_f W^2 C_{s0}}{D_i C_{i0}}, \quad (21b)$$

which indicate the relative rates of the chemical reactions given by (1) with respect to diffusion.

The coupled equations (20) can be simplified, first noting that adding (20a) and (20b) leads to

$$\frac{1}{Da_s} \frac{d^2 c_s}{dy^2} + \frac{1}{Da_i} \frac{d^2 c_i}{dy^2} = 0. \quad (22)$$

We can then differentiate (20b) twice and combine it with (22) to obtain

$$\frac{d^4 c_i}{dy^4} = Da_i \frac{d^2 (c_i^\nu)}{dy^2} + Da_s \frac{d^2 c_i}{dy^2}, \quad (23)$$

thereby reducing the coupled system to a single fourth-order nonlinear equation for c_i , whose solution requires four boundary conditions to be determined uniquely.

In the case of *liquid sources*, the boundary conditions are the nondimensional versions of (8) and (9) for the solute and ions, respectively. Combining those expressions with (20b), it is possible to cast the four boundary conditions in terms of c_i only, leading to

$$c_i = 1 \quad \text{at } y = 0, \quad (24a)$$

$$c_i = \varepsilon^{1/\nu} \quad \text{at } y = 1, \quad (24b)$$

$$\frac{d^2 c_i}{dy^2} = 0 \quad \text{at } y = 0 \text{ and } y = 1, \quad (24c)$$

where we define $\varepsilon := C_{s*}/C_{s0} = (C_{i*}/C_{i0})^\nu$ as the ratio of solute concentration between the sink and the source. Since, in practice, the sink could be engineered to have a very low concentration such that $\varepsilon \ll 1$, taking $\varepsilon = 0$ would seem as a natural simplification. However, in the

particular case of liquid sources, a “perfect” sink with $\varepsilon = 0$ would lead to a zero concentration $c_i(1) = 0$ at the wall and, as a consequence, to a divergent particle velocity $|v_p| \rightarrow \infty$, according to (17). This would in turn result in an unbounded distribution $n_-(y)$ of particles in the case in which they are chemo-repelled, highlighting that a small (but nonzero) value of ε has an effect that is not small in the case of a liquid source. While it is possible to regularize this divergence including other physical effects like a concentration-dependent mobility⁴¹, here we will simply assume a nonzero value $0 < \varepsilon < 1$ in the case of a liquid source.

In the case of *gas sources*, the boundary conditions are the nondimensional versions of (8) and (11), which can once again be combined with (20b) to arrive at

$$c_i^\nu - \frac{1}{Da_i} \frac{d^2 c_i}{dy^2} = 1 \quad \text{at } y = 0, \quad (25a)$$

$$c_i^\nu - \frac{1}{Da_i} \frac{d^2 c_i}{dy^2} = 0 \quad \text{at } y = 1, \quad (25b)$$

$$\frac{dc_i}{dy} = 0 \quad \text{at } y = 0 \text{ and } y = 1, \quad (25c)$$

where we have taken $\varepsilon = 0$ since, in this case, the limit does not lead to a singular particle velocity because the no-flux condition (25c) prevents c_i from becoming zero at the sink. This means that imperfect sinks with small values $0 < \varepsilon \ll 1$ have only small, higher-order effects on the particle distribution in the case of gas sources.

Neither the boundary-value problem for liquid sources, given by (23) and (24), nor the one for gas sources, given by (23) and (25), are exactly solvable in general. However, we can obtain key insights about the structure of their solutions from an asymptotic analysis^{42–44} of the problem in practically relevant physical regimes. To that end, we first estimate the typical ranges of values of the three dimensionless numbers (Pe_p , Da_s , and Da_i) to identify different distinguished limits in the parameter space.

Estimation of parameters. In order to estimate the Péclet number Pe_p , the particle diffusivity D_p can be calculated using the Stokes-Einstein relation $D_p = k_B T / (6\pi\mu R_p)$, with k_B the Boltzmann constant, T the absolute temperature, μ the dynamic viscosity of the medium, and R_p the particle radius. This formula neglects electrostatic effects and is strictly valid only in the limit of a thin double layer compared to the particle size $\lambda_D \ll R_p$, but is nevertheless useful as an order-of-magnitude estimate. For water at room temperature, and for particle sizes in the range $R_p = O(10 \text{ nm} - 10 \mu\text{m})$ relevant in practice, we have diffusivities $D_p = O(10^{-11} - 10^{-14} \text{ m}^2/\text{s})$. In turn, at moderate concentrations $C_{i0} = O(0.1 - 10 \text{ mM})$ we can expect diffusiophoretic mobilities Γ_p to be of the same order of magnitude as the ambipolar diffusivity of the electrolyte⁴¹. Most small-molecule substrates in aqueous solutions have $D_i = O(10^{-10} - 10^{-9} \text{ m}^2/\text{s})$, so we expect that $Pe_p = |\Gamma_p|/D_p = O(10^2 - 10^4)$. Therefore, we only consider the relevant asymptotic

limit of $Pe_p \gg 1$. This range of values of Pe_p should not come as a surprise, since diffusiophoresis is sought in applications precisely because it overcomes Brownian motion, inducing the directed migration of colloids^{7,14,16}.

Estimating the values of the two Damköhler numbers is more challenging due to the wide range of variation of the kinetic constants k_f and k_r . Nevertheless, we can distinguish qualitatively between two limiting key regimes, given that the ratio of Damköhler numbers (21) yields

$$\frac{Da_i}{Da_s} = \frac{D_s}{D_i} \frac{C_{s0}}{C_{i0}}. \quad (26)$$

Since we can expect D_s and D_i to be of the same order of magnitude, the quantity Da_i/Da_s essentially indicates how displaced is the chemical equilibrium given by (1). If $Da_i \ll Da_s$, then ionic concentrations are dominant, $C_{i0} \gg C_{s0}$, and the dissociation is *strong*. Conversely, if $Da_i \gg Da_s$, then $C_{i0} \ll C_{s0}$ and the dissociation is *weak*. Figure 2 displays the numerical solution of the problem (23) for $\nu = 2$, $Pe_p \gg 1$, in both the weak and strong dissociation limits, and using either boundary conditions (24) for a liquid source (Figure 2a-c) or (25) for a gas source (Figure 2b-d). We use $Da_s = 1$ in all cases, $Da_i = 1/50$ for weak dissociation, and $Da_i = 50$ for strong dissociation, which are chosen as a representative set of values to capture each regime qualitatively. Additionally, we pick $\varepsilon = 0.1$ to regularize the cases with a liquid source and $\varepsilon = 0$ for gas sources. Note that the concentration and particles have noticeably different spatial distributions depending on the boundary conditions and the regime of dissociation.

In the next three subsections, we analyze the asymptotic structure of the problem to obtain quantitative predictions for the separation efficiency. We seek to obtain the simplest possible leading-order expression for the particle distributions $n_{\pm}(y)$ as a function of Pe_p , Da_i , Da_s (and, in the case of liquid sources, also ε), neglecting all higher-order effects.

Particle distributions at $Pe_p \gg 1$

We first analyze the exact solutions for the distribution of particles given by (19), in the relevant case of $Pe_p \gg 1$. In this limit, we can expect $n_{\pm}(y)$ to have a *boundary layer* structure^{42,43}, with particles accumulating in thin regions near walls. We denote the width of these regions as δ_{\pm} , for the chemo-attracted particles accumulating at the chemical source, and δ_{-} , for the chemo-repelled particles accumulating at the chemical sink. For high enough Péclet number, these regions can get thin enough to approximate the ionic concentration $c_i(y)$ by its leading-order Taylor expansion, since deviations only become noticeable outside the boundary layers δ_{\pm} . We

first introduce local coordinates

$$y_+ = y \quad (27a)$$

$$y_- = 1 - y, \quad (27b)$$

to use a more compact notation that ensures $y_{\pm} = 0$ at either wall, and then pose a linear expansion

$$c_i(y_{\pm}) = c_i(0) + \frac{dc_i}{dy_{\pm}}(0) y_{\pm} + O(y_{\pm}^2) \quad (28)$$

in the case of a liquid source, and a quadratic expansion

$$c_i(y_{\pm}) = c_i(0) + \frac{d^2 c_i}{dy_{\pm}^2}(0) \frac{y_{\pm}^2}{2} + O(y_{\pm}^3) \quad (29)$$

for gas sources, since in that case we have no ionic flux at walls as given by (25c). Introducing these expansions into the solution (19) for the particles, and after an asymptotic analysis that we detail in the Supplementary Material, we can show that, neglecting all exponentially small terms, the leading-order approximations $n^{(0)}$ for the particles are

$$n_{\pm}^{(0)}(y_{\pm}) = \frac{e^{-y_{\pm}/\delta_{\pm}}}{\delta_{\pm}} \text{ for liquid sources, and} \quad (30a)$$

$$n_{\pm}^{(0)}(y_{\pm}) = \frac{2e^{-(y_{\pm}/\delta_{\pm})^2}}{\sqrt{\pi} \delta_{\pm}} \text{ for gas sources.} \quad (30b)$$

The analysis also allows us to identify and define the widths δ_{\pm} of the particle boundary layers, which we obtain as

$$\delta_{\pm} = \frac{c_i(0)}{\left| \frac{dc_i}{dy_{\pm}}(0) \right|} Pe_p^{-1} \text{ for liquid sources,} \quad (31a)$$

$$\delta_{\pm} = \left[\frac{2c_i(0)}{\left| \frac{d^2 c_i}{dy_{\pm}^2}(0) \right|} \right]^{1/2} Pe_p^{-1/2} \text{ for gas sources,} \quad (31b)$$

where we emphasize that the values of c_i and its derivative are evaluated at walls $y_{\pm} = 0$ or, equivalently, at either $y = 0$ (for the “+” case) or $y = 1$ (for “-”).

In summary, the particle distributions in the limit of large particle Péclet number will tend to either exponential (30a) or Gaussian (30b) curves near channel walls, depending on whether the chemical source delivers a liquid or a gas. Furthermore, these distributions and, by extension, the separation of colloids, is dictated by a single boundary layer parameter δ_{\pm} at each wall, which itself depends on the ionic concentration through Equation (31). In the next two subsections, we evaluate the concentration profiles $c_i(y)$ and their relevant Taylor expansions near walls to obtain δ_{\pm} using (31).

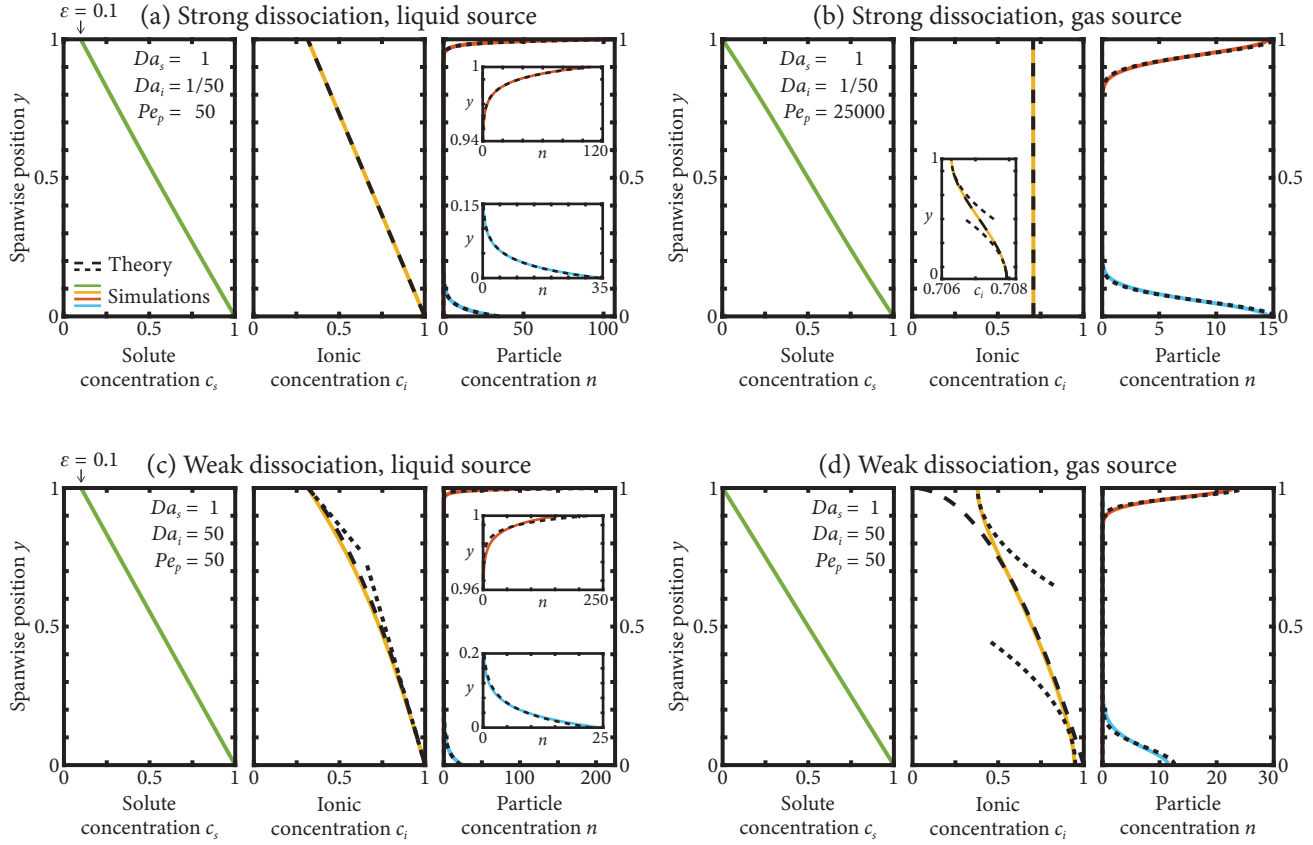


Figure 2: Colloid separation through diffusiophoresis strongly depends on the dissociation chemistry and type of permeating membrane. Each sub-figure represents: (a) $Da_i \ll 1$, ions equilibrated with reservoirs [Eqs. (24)], (b) $Da_i \ll 1$, no ionic wall flux [Eq. (25)], (c) $Da_i \gg 1$, ions equilibrated with reservoirs [Eq. (24)], (d) $Da_i \gg 1$, no ionic wall flux [Eq. (25)].

Strong dissociation ($Da_i \ll Da_s$)

Here, we assume an order-one value of $Da_s = O(1)$, while taking a small $Da_i \ll 1$ such that $Da_i/Da_s \ll 1$. Accordingly, we expand c_i in powers of Da_i as

$$c_i = c_i^{(0)} + Da_i c_i^{(1)} + O(Da_i^2) \quad (32)$$

in the governing equation (23). At leading-order, we obtain a linear ODE

$$\frac{d^4 c_i^{(0)}}{dy^4} = Da_s \frac{d^2 c_i^{(0)}}{dy^2} \quad (33)$$

that results in a different ionic profile $c_i^{(0)}(y)$ depending on the specific boundary conditions, as we show next.

Liquid sources. Solving (33) subject to boundary conditions (24) results in a linear profile

$$c_i^{(0)}(y) = 1 - (1 - \varepsilon^{1/\nu})y, \quad (34)$$

which, as displayed in the central panel of Figure 2a, is indistinguishable from the full numerical solution of (23). We can then easily obtain the Taylor expansions $c_i(y_+) = 1 - (1 - \varepsilon^{1/\nu})y_+$ and $c_i(y_-) = \varepsilon^{1/\nu} + (1 - \varepsilon^{1/\nu})y_-$

at both walls which, when introduced in (31), lead to

$$\delta_+ = \frac{1}{1 - \varepsilon^{1/\nu}} Pe_p^{-1}, \quad (35a)$$

$$\delta_- = \frac{\varepsilon^{1/\nu}}{(1 - \varepsilon^{1/\nu})} Pe_p^{-1}. \quad (35b)$$

The solutions resulting from using (35) in the profiles given by (30) are plotted in the right panel of Figure 2a, showing good agreement with the numerical results. The formulae (35) highlight the *boundary layer* structure, with widths $\delta_+ \ll 1$ and $\delta_- \ll 1$ that are small since $Pe_p \gg 1$ and $\varepsilon < 1$, which can be confirmed graphically in Figure 2a. This spatial distribution is precisely what is sought to optimize the efficiency of separation and maximize the output of clean water (the filtrate) with respect to the total influx of contaminated water (the feed). In the case of chemo-repelled particles, accumulation is enhanced due to the lower ionic concentration $c_i(1)$ at the chemical sink, which in turn leads to a higher diffusiophoretic velocity. This is apparent from the fact that the expressions for the boundary layer thicknesses (35) are identical except for an extra factor of $\varepsilon^{1/\nu} < 1$, making $\delta_- < \delta_+$ and the chemo-repelled particles accumulate more strongly at the top ($y = 1$) wall, as shown by Figure 2a. In

fact, as $\varepsilon \rightarrow 0$ and the membrane becomes a perfect sink, the boundary layer thickness δ_- tends to zero and the particle distribution becomes singular, emphasizing the strong effect of ε . Note also that in this particular case the separation does not depend on the reaction chemistry at leading order, given that δ_+ and δ_- do not depend on Da_s or Da_i .

Gas sources. We proceed by solving (33) with boundary conditions (25) for gas sources. At leading order in Da_i , the solution is $c_i^{(0)}(y) = A$, with A some undetermined constant. This result highlights that this case is characterized by very mild gradients giving a constant ionic concentration and therefore a zero particle velocity at leading order. Physically, this can be understood by noting that the strong dissociation depletes the solute and drives the vast majority of the chemical into the ions which, owing to their no-flux conditions at both walls, tend to a flat profile. The numerical solution plotted in the inset of Figure 2b, however, reveals some very mild gradients, which can only be captured by solving for $c_i^{(1)}(y)$ in the first-order problem. A detailed calculation (see the Supporting Information) leads to

$$c_i^{(0)}(y) = 2^{-1/\nu}, \quad (36a)$$

$$c_i^{(1)}(y) = -\frac{\left[y - \frac{1}{2} + \frac{e^{\sqrt{Da_s}(1-y)} - e^{\sqrt{Da_s}y}}{\sqrt{Da_s}(1+e^{\sqrt{Da_s}})}\right]}{2Da_s^{1/2} \tanh(\sqrt{Da_s}/2)}, \quad (36b)$$

with the approximate first-order solution $c_i^{(0)} + Da_i c_i^{(1)}$ plotted with a dashed line in Figure 2b and showing excellent agreement with the numerical simulations. It is now straightforward to obtain local expansions of c_i at walls, which are now parabolic and displayed with dotted lines in the inset of Figure 2b. Introducing these expansions in (31), we obtain

$$\delta_+ = \delta_- = 2^{\frac{2\nu-1}{2\nu}} Pe_p^{-1/2} Da_i^{-1/2}. \quad (37)$$

A closer look at (37) shows that particle distributions are symmetric and, since $Da_i \ll 1$ in this case, the Péclet number must be very large for the boundary layers δ_+ and δ_- to be small. In fact, a detailed analysis (see the Supporting Information) reveals that $Pe_p \gg Da_i^{-1}$ to have noticeable particle accumulation. Indeed, in Figure 2 all cases display noticeable particle accumulation for a moderately large $Pe_p = 50$ except for strong dissociation and gas sources, for which $Pe_p = 25000$ to have accumulation comparable to the other three scenarios. This is, once again, a direct consequence of the weak gradients that appear in this case, which strongly limits the feasibility of the separation and suggests that gases with very fast dissociation reactions must be avoided in practice.

Weak dissociation ($Da_i \gg Da_s$)

We now keep an order-one value of $Da_s = O(1)$ but take a large $Da_i \gg 1$ such that $Da_i/Da_s \gg 1$. Accordingly, we pose an expansion

$$c_i = c_i^{(0)} + Da_i^{-1} c_i^{(1)} + O(Da_i^{-2}) \quad (38)$$

in (23) which, at leading-order, yields

$$\frac{d^2}{dy^2} \left[\left(c_i^{(0)} \right)^\nu \right] = 0. \quad (39)$$

This equation can be integrated to obtain the solution $c_i^{(0)} = [K_1 + K_2 y]^{1/\nu}$, with K_1 and K_2 integration constants. Since, in general, one cannot impose the four required boundary conditions given by either (24) or (25) with only two constants, c_i also has a boundary layer structure. The leading-order equation (39) is therefore only an “outer” equation not valid sufficiently close to the walls, where other terms must become non-negligible to ensure all boundary conditions are satisfied. We tackle this boundary layer problem through the method of matched asymptotic expansions^{42–44}, with all the details available in the Supporting Information, and outline the results in the next two subsections.

Liquid sources. In this case, two boundary layers of width $l_+ = l_- = O(Da_i^{-1/2})$ form at each wall, with two corresponding “inner” linear ODEs that can be formulated in these regions. Note the contrast between the *chemical* boundary layers l_\pm for $c_i(y)$ and the particle boundary layers δ_\pm for $n(y)$, which scale differently. The solution to these inner problems can be matched to the outer solution $c_i^{(0)} = [K_1 + K_2 y]^{1/\nu}$ to obtain the constants, leading to $c_i^{(0)} = [1 - (1 - \varepsilon) y]^{1/\nu}$, which is displayed with dashed lines in Figure 2c. As in previous cases, we only seek to find local expansions of $c_i(y)$ near walls, obtaining

$$c_i \approx 1 - \frac{1 - \varepsilon}{\nu} y_+ \quad \text{at the source,} \quad (40a)$$

$$c_i \approx \varepsilon^{1/\nu} + \frac{\varepsilon^{\frac{1-\nu}{\nu}} (1 - \varepsilon)}{\nu} y_- \quad \text{at the sink,} \quad (40b)$$

which are plotted as dotted lines in Figure 2c. Introducing these expressions in (31), we obtain

$$\delta_+ = \left(\frac{\nu}{1 - \varepsilon} \right) Pe_p^{-1}, \quad (41a)$$

$$\delta_- = \left(\frac{\nu \varepsilon}{1 - \varepsilon} \right) Pe_p^{-1}. \quad (41b)$$

These expressions depend on the reaction order (with wider layers for larger ν), but are still independent of kinetics since Da_i and Da_s do not appear in (41). As in the case of a strong dissociation with a liquid source, the boundary layer δ_- also vanishes as $\varepsilon \rightarrow 0$, although in this case the effect of a small concentration at the

sink is stronger given that δ_- depends on ε as opposed to $\varepsilon^{1/\nu}$. This is evident comparing the chemo-repelled particle distribution in Figures 2a and 2c, with the latter reaching larger particle accumulation near the sink wall.

Gas sources. The last case involves a gas source and weak dissociation, with CO₂-driven diffusiophoresis as a prominent example^{24,26,35,36}. Matched asymptotics reveals that the boundary layer at the source is governed by a linear inner equation with $l_+ = O(Da_i^{-1/2})$, while at the sink the inner equation is nonlinear and leads to $l_- = O(Da_i^{-\nu/(3\nu-1)})$. The full analysis (see the Supporting Information) yields the local expansions

$$c_i \approx 1 - \frac{Da_i^{-1/2}}{\nu^{3/2}} - \frac{Da_i^{1/2}}{2\nu^{1/2}} y_+^2 \quad \text{at the source,} \quad (42a)$$

$$c_i \approx \alpha Da_i^{\frac{-1}{3\nu-1}} + \frac{\alpha^\nu}{2} Da_i^{\frac{2\nu-1}{3\nu-1}} y_-^2 \quad \text{at the sink,} \quad (42b)$$

plotted with dotted lines in Figure 2d. The constant α cannot be calculated in closed form due to the nonlinear inner problem, but can be easily obtained by numerically solving the boundary-value problem

$$\frac{d^2 f}{d\xi^2} = f^\nu - \xi, \quad (43a)$$

$$\frac{df}{d\xi} = 0 \quad \text{at } \xi = 0, \quad (43b)$$

$$f \rightarrow \xi^{1/\nu} \quad \text{as } \xi \rightarrow \infty, \quad (43c)$$

to then take $\alpha = f(0)$. Note that while the reaction order ν appears in (43), the constant α has a very weak dependence on ν , as shown in Table 1.

Introducing the parabolic local expansions (42) into (31) leads to boundary layer widths given by

$$\delta_+ = \left(2^{1/2}\nu^{1/4}\right) Da_i^{-1/4} Pe_p^{-1/2}, \quad (44a)$$

$$\delta_- = \left(2^{1/2}\alpha^{\frac{1-\nu}{2}}\right) Da_i^{-\frac{\nu}{3\nu-1}} Pe_p^{-1/2}. \quad (44b)$$

In this case, the boundary layers clearly depend on the dissociation kinetics through the Damköler number, with different power laws in each wall that highlight the problem asymmetry.

In addition, in the case of chemo-attracted particles we find the additional requirement $Pe_p \gg Da_i^{1/2}$ for the model to be valid, since otherwise the particle boundary layer is not contained within the chemical boundary layer (i.e. $\delta_+ \ll l_+$ is not satisfied), and the

Table 1: Values of the exponent $-\nu/(3\nu-1)$ and the constant α (obtained numerically) appearing in (42b) and (44b), as a function of the reaction order ν .

ν	2	3	4	5
$-\frac{\nu}{3\nu-1}$	-2/5	-3/8	-4/11	-5/14
α	0.830965	0.839455	0.855196	0.869162

underlying approximations of the model break down. In the case of chemo-repelled particles, however, we find that the scalings are such that this situation can never occur, so any value of $Pe_p \gg 1$ is valid. More details about these conditions can be found in the Supplementary Material.

Water recovery

Equipped with a quantitative theory to predict the accumulation of colloidal particles, we can now compute metrics relevant for colloid separation. We first focus on the *water recovery*, typically defined in the literature⁴⁵ as the proportion of freshwater that can be obtained from the contaminated feed which, as discussed above, has a (dimensionless) mean particle concentration of 1. Defining the freshwater stream as the region within the channel with particle concentration below a reference value $n(y) < n_{\text{ref}}$, we can obtain the water recovery γ by plugging $n(y_{\text{ref}}) = n_{\text{ref}}$ into the expressions (30a) or (30b) for the particle distributions, with y_{ref} some position where the particle concentration reaches the reference concentration. Then, noting that $\gamma = 1 - y_{\text{ref}}$ for chemo-attracted particles, while $\gamma = y_{\text{ref}}$ if they are chemo-repelled, we can solve for γ . The result is

$$\gamma = 1 - \delta_\pm \log \left[\frac{1}{\delta_\pm n_{\text{ref}}} \right] \quad \text{for liquid sources, and} \quad (45a)$$

$$\gamma = 1 - \delta_\pm \log^{1/2} \left[\frac{2}{\sqrt{\pi} \delta_\pm n_{\text{ref}}} \right] \quad \text{for gas sources.} \quad (45b)$$

Microfluidic Experiments

Materials and methods

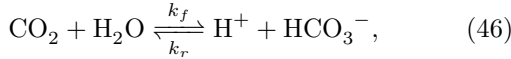
We fabricate microfluidic devices using standard soft lithography, where PDMS (Sylgard 184, Dow Corning) with a 10:1 ratio of elastomer base to curing agent is poured over a mold of SU-8 resin (SU-8 2050, Kayaku Advanced Materials) fabricated via photolithography. After curing, the solid polymer is peeled from the mold and bonded to a glass slide where a thin PDMS film has previously been spin-coated and cured. This setup ensures that all channel walls are made of PDMS, preventing any asymmetries in surface chemistry.

The chip, shown schematically in Figure 3a, consists of three parallel channels of nominal height and width of $H = 40 \mu\text{m}$ and $W = 250 \mu\text{m}$, respectively. Flows of pure carbon dioxide and nitrogen gas are driven along the two side channels, while a suspension of deionized water (Direct Q3, Millipore) and fluorescent micro-particles is injected into the central channel using a syringe pump (Pump 11 Pico Plus Elite, Harvard Apparatus). The channels are separated by walls of thickness $w = 100 \mu\text{m}$ along a segment of length $L = 55 \text{ mm}$, over which the natural permeability of the polymer to gases⁴⁶ allows the CO₂ to permeate from the “source” channel, dissolve and diffuse across

the water, and then permeate again into the flowing nitrogen at the “sink”, replicating the setup outlined in Figure 1 with a monolithic, easy-to-fabricate PDMS chip^{22,24,26,35,36}. The sustained flow in all three channels ensures a persistent flux of dissolved CO₂ in the spanwise direction, preventing the saturation of the sink with CO₂ over time.

We note that even though our experiments are three-dimensional (with a channel height H that introduces vertical confinement) and the theory is formulated in two dimensions, they are still comparable. While vertical variations in the flow speed and subsequent Taylor dispersion induces vertical changes in the developing c_s , c_i , and n profiles, as shown by Shim et al.²⁴, in the fully-developed case streamwise advection is zero and this effect is non-existent. Furthermore, since the fluxes of solute, ions and particles through the top and bottom walls of the channels are either zero or can be assumed negligible compared to those through the sink and source side walls, we expect the c_s , c_i , and n profiles to be truly invariant in x , provided they have fully developed.

All experiments are performed setting a gauge pressure of $p_{in} = 1.38 \cdot 10^4$ Pa for both CO₂ and N₂ at the channel inlets, which leads to a concentration of $C_{s0} \approx 29.5$ mM of CO₂ dissolved in water at the “source” wall (see the Supplementary Material). We then expect the CO₂ dissolve in water through the dissociation reaction



which sets the parameter $\nu = 2$ from the reaction stoichiometry. Using well-characterized values of the reaction rate constants⁴⁷ k_f and k_r , we can estimate the scale for the ionic concentration $C_{i0} \approx 0.118$ mM and the Damköhler numbers, as defined in Equation (21), $Da_s \approx 1.28$ and $Da_i \approx 306$ in all experiments. These values correspond to the “weak dissociation” regime, as detailed in the Theory section above, and therefore do not replicate all the different theoretical regimes analyzed. Instead, the experiments focus on validating the specific case of a chemical source with a weakly dissociating gas. Since gas sources with a strong dissociation are predicted by our theory to yield a very low separation efficiency, we expect that the regime in the experiments is the most practically relevant to induce separation through diffusiophoresis using gases. In addition, under these conditions we can estimate the Debye length $\lambda_D \approx 29$ nm, much smaller than any of the channel dimensions or particle sizes used.

We probe suspensions of three different types of particles: amine-modified polystyrene (a-PS), carboxylate-modified polystyrene (c-PS), and uncoated polystyrene (PS). Two different particles sizes are used for each of the three types, with their properties summarized in Table 2, allowing us to span a broad range of particle Péclet numbers in both chemo-attracted and chemo-repelled colloids. Since the

particles size include small diameters below hundreds of nanometers, and since the ionic concentration is relatively low, we compute the mobilities Γ_p using the full expressions derived by Prieve et al.⁵, which depend on both the particle size and the electrolyte concentration. The implications of choosing this model for the mobilities, which assumes a binary electrolyte and a constant potential on the particle, are discussed by Gupta et al.⁴¹. As opposed to the a-PS and PS particles, the c-PS particles increase their Γ_p in absolute value as the particle size decreases. The trend, opposite for all other particle types, can occur for highly negatively-charged particles due to a subtle interplay between the electrophoretic and chemiphoretic contributions to the mobility²⁶. Particle diffusivities D_p are calculated from the Stokes-Einstein relation⁴⁸. In the experiments with amine-modified particles, we pump a 1 vol% aqueous solution of 3-aminopropyltriethoxysilane (APTES) for 15 minutes prior to injecting the particle suspension to prevent particle adhesion with the PDMS walls^{25,26}. We use suspensions with a particle volume fraction of $\phi \approx 1.5 \cdot 10^{-4}$ in all experiments.

Experimental protocol

We use an inverted fluorescence microscope (Leica DMI4000B) to image the central channel during a time interval of approximately 20 s, at either 10X or 20X magnification (window sizes of 1424×1064 μm and 712×532 μm , respectively). A typical acquisition image is shown in Figure 3b, for the case of 0.1 μm -diameter c-PS particles. We use the fluorescence signal of the particles (displayed in white) as a proxy for their concentration, ensuring that the signal does not change appreciably during the acquisition time and is therefore in a steady state. For each type and size of particles, we also run a calibration test without CO₂ or N₂ to corroborate that the measured fluorescent signal changes linearly with concentration for the range of particle volume fractions that considered, as detailed in the Supplementary Material.

As shown in Figure 3b, particles accumulate at the (top) sink wall, as expected for this particular case of chemo-repelled particles with a negative mobility Γ_p . Since our goal is to capture the fully-developed regime where particle profiles are invariant in the streamwise X direction, we fix the acquisition window at the end of the channel ($X \approx 55$ mm), and progressively decrease the flow rate to reach the fully-developed limit. Note that the flow rates used, shown in Figure 3b, are small (with $Q = 0.0625 - 1 \mu\text{L}/\text{min}$) since experiments are constrained by the typical length of a glass slide (around 75 mm). In practically relevant scenarios, channel dimensions could be tuned to maximize flow rate while ensuring that the fully developed regime can be achieved within a feasible channel length, following the analysis in Shim et al. of the developing particle profiles.

Given that the width of the acquisition windows

Table 2: Comparison of different particle properties used in the experiments.

Particle type	Amine-modified (a-PS)		Carboxylate-modified (c-PS)		Uncoated (PS)	
Diameter [μm]	1	0.2	1	0.1	1.04	0.08
Zeta potential ζ_p [mV]	60		-75		-50	
Mobility Γ_p [m^2/s]	$7.5 \cdot 10^{-10}$	$3.2 \cdot 10^{-10}$	$-6.1 \cdot 10^{-10}$	$-1.0 \cdot 10^{-9}$	$-4.6 \cdot 10^{-10}$	$-2.9 \cdot 10^{-10}$
Diffusivity D_p [m^2/s]	$4.4 \cdot 10^{-13}$	$2.2 \cdot 10^{-12}$	$4.4 \cdot 10^{-13}$	$4.4 \cdot 10^{-12}$	$4.2 \cdot 10^{-13}$	$5.4 \cdot 10^{-12}$
Péclet number Pe_p	$1.7 \cdot 10^3$	$1.5 \cdot 10^2$	$1.4 \cdot 10^3$	$2.4 \cdot 10^2$	$1.1 \cdot 10^3$	$5.3 \cdot 10^1$

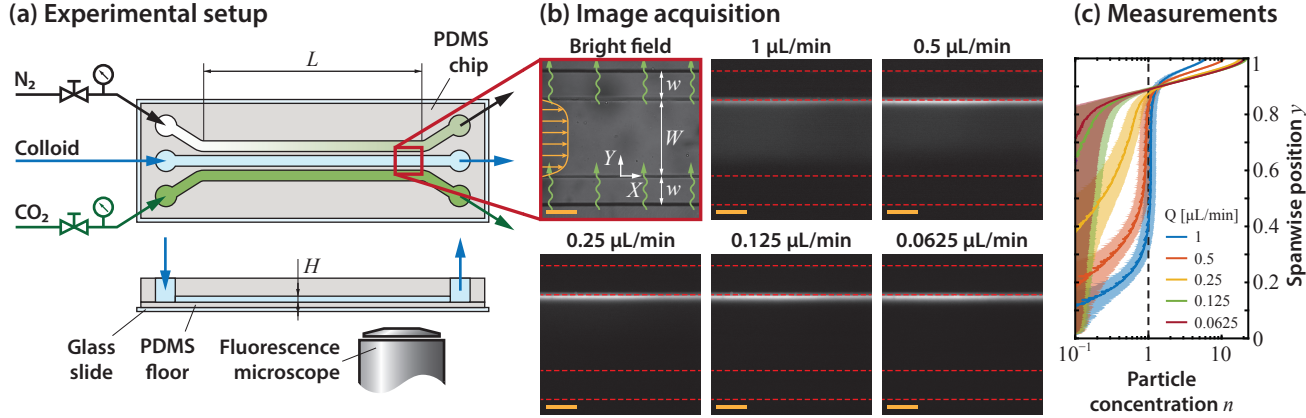


Figure 3: Microfluidic experiments reproduce the regime of fully-developed particle concentrations using CO_2 -driven diffusiophoresis. (a) Sketches of the top view and cross-section of the microfluidic devices. (b) Bright-field image of the acquisition window, followed by the fluorescent signal acquired at steady state for five different flow rates. Note that the white particles (in this example, c-PS particles of diameter $0.1 \mu\text{m}$) progressively accumulate at the top wall (i.e. the sink) with a decreasing flow rate. Error bars on the bottom left corner correspond to $100 \mu\text{m}$. (c) Corresponding fluorescent signal, normalized to yield a mean value of 1 (dashed line). Error bars indicate the standard deviation obtained from averaging the signal in time and in the streamwise direction. The data shows a thin particle-free boundary layer (i.e. an “exclusion zone”) near the source of CO_2 that grows with a decreasing flow rate. The two curves with the lowest flow rates display a statistically negligible discrepancy, demonstrating that they correspond to the “fully-developed” regime of interest.

is much smaller than the channel length $L \approx 55 \text{ mm}$ over which the particle concentration evolves in the streamwise direction, we average the fluorescence signal in X across the acquisition window, as well as in time. The result, normalized to ensure a unit mean concentration, is plotted in Figure 3c. For the highest three flow rates, the particle profiles are clearly still developing in the streamwise direction: they display a distinct particle free-exclusion zone near the (bottom) source wall, followed by a region of constant particle concentration in the intermediate section of the channel. This constant value is roughly the average $n \approx 1$ incoming from the inlet, reinforcing our interpretation of a developing particle profile with a boundary-layer structure²⁴. In addition, these developing particle profiles display a peak at the (top) sink wall, which we attribute to the dissolved CO_2 naturally present in the water diffusing into the absorbing sink. The particle profiles for the lowest two flow rates have no meaningful statistical difference, as evidenced in Figure 3c. This fact confirms that the profile has fully developed and that it can be compared against our theoretical model. The same process of varying the flow rate until a fully-developed profile is identified is followed for all

experiments, such that only the fully-developed profiles are compared to our theory.

Results for fully-developed particles

The fully-developed particle profiles obtained in six representative experiments are displayed in Figure 4a. Each of the six cases corresponds to particles of a different type or size, and is normalized to ensure a unit mean $\int_0^1 n \, dy = 1$. In order to compare the profiles to the model, we focus on the maximum concentration $n_{\max} = n_{\pm}(y_{\pm} = 0)$ at the walls, since a metric like the water recovery in Equation (45), while highly relevant in practice, depends on an arbitrary reference particle concentration n_{ref} that is difficult to measure experimentally. From Equation (30b) and the expressions (44) for δ_{\pm} , we expect from theory that $\delta_{\pm} = 2/(\sqrt{\pi}\delta_{\pm})$ and that

$$n_{\max} = \frac{2^{1/4}}{\pi^{1/2}} Da_i^{1/4} Pe_p^{1/2} \text{ at the source,} \quad (47a)$$

$$n_{\max} = \left(\frac{2\alpha}{\pi} \right)^{1/2} Da_i^{2/5} Pe_p^{1/2} \text{ at the sink.} \quad (47b)$$

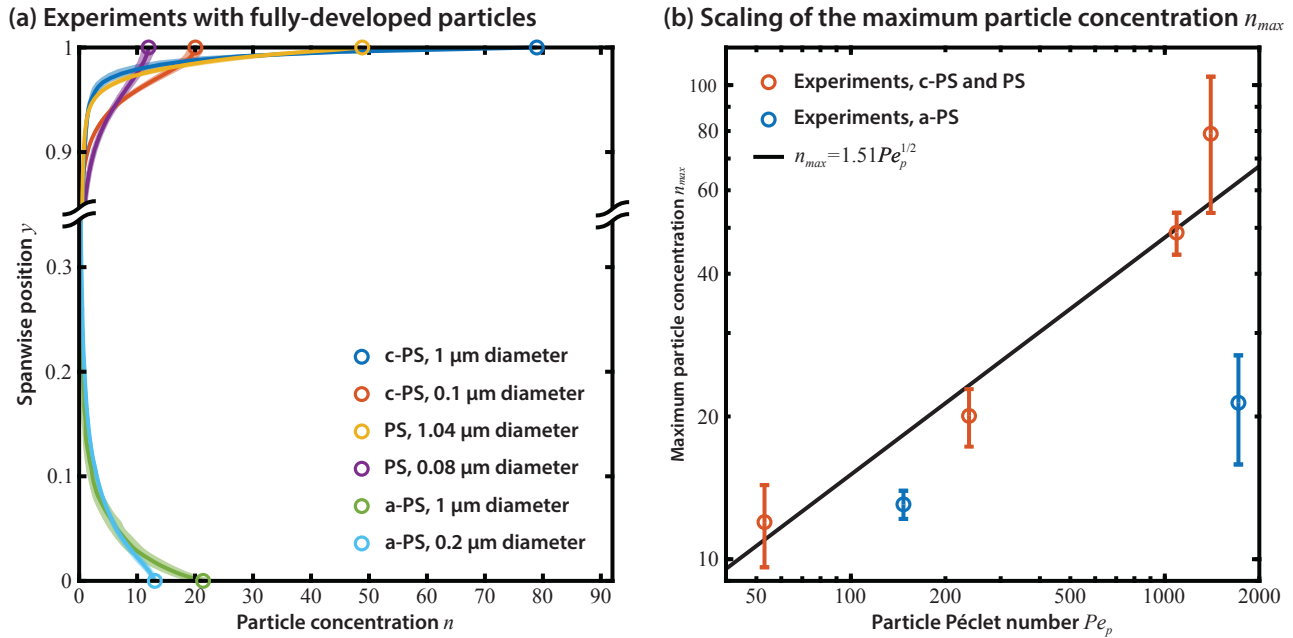
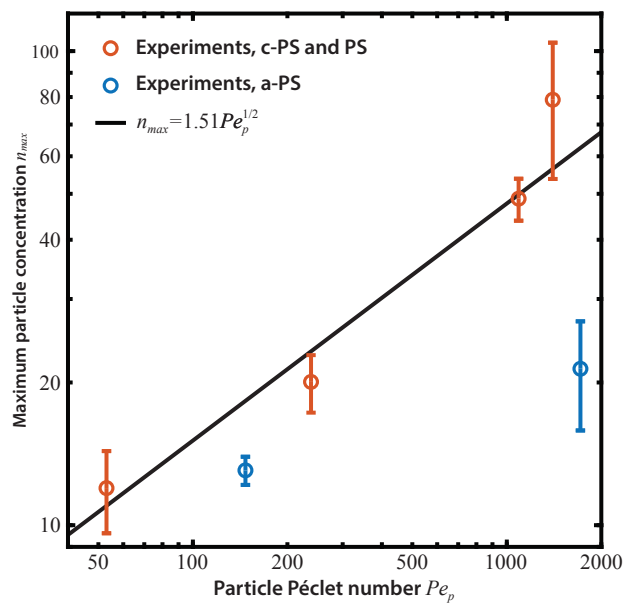


Figure 4: Experimental measurements of fully-developed particle profiles reproduce the scaling predicted by theory. (a) Fluorescent signal, normalized to yield a mean value of 1, for fully-developed profiles of particles of different types and sizes, as detailed in Table 2. (b) Maximum particle concentration n_{max} (at walls $y = \pm 1$) as a function of the particle Péclet number Pe_p , as defined in Equation (16). Note the trend $n_{max} \propto Pe_p^{1/2}$, predicted by theory, for chemo-repelled particles (c-PS and PS). For chemo-attracted particles (a-PS), the available experimental data displays significantly lower values of n_{max} , agreeing qualitatively with theory.

Qualitatively, we can expect that particles with a higher Pe_p will display higher n_{max} , and that chemo-attracted particles will achieve lower concentrations than chemo-repelled particles at the same values of Pe_p since, comparing the prefactors, $Da_i^{2/5} > Da_i^{1/4}$. This qualitative trend is reproduced in Figure 4a, where all particle types show a monotonic increase in n_{max} with Pe_p , and where the chemo-repelled c-PS and PS particles show higher accumulation than the chemo-attracted a-PS particles.

The scaling $n_{max} \propto Pe_p^{1/2}$ is also reproduced quantitatively for the four types of chemo-repelled particles, as shown in Figure 4b. While the availability of only two types of chemo-attracted particles precludes drawing any quantitative conclusion, the measured value of n_{max} is also consistently lower than the expected value for chemo-repelled particles of the same Pe_p . It is worth noting that the prefactor of approximately 1.5 obtained from fitting the experimental data for chemo-repelled particles deviates from the expected value of $\sqrt{2\alpha/\pi} Da_i^{2/5} \approx 7.1$ by a factor of approximately 4.7. Such a deviation could originate from complexities in the charge dynamics at the particles, such as charge regulation mechanisms⁴⁹, or from more complex reaction chemistry that is not captured by the single-reaction mechanism (46).

(b) Scaling of the maximum particle concentration n_{max}



Discussion

The quantitative theory presented here is naturally subject to a number of limitations, the first being that it assumes a binary electrolyte generated by an elementary dissociation reaction given by Equation (1). While multi-ion electrolytes where concentrations of more than two species are non-negligible would introduce significant differences in the governing equations, complex reaction mechanisms, as long as they can be approximated by an *effective* single reaction of the form (1), would still be captured. Such effective reactions could arise, for instance, with the disparity of different reaction timescales that can be simplified using the well-known quasi-steady-state approximation (QSSA) in chemical kinetics. In fact, the dissociation of carbon dioxide given by (46) proceeds in two steps $\text{CO}_2 + \text{H}_2\text{O} \rightleftharpoons \text{H}_2\text{CO}_3 \rightleftharpoons \text{H}^+ + \text{HCO}_3^-$, which can be approximated⁵⁰ by the single reaction step given by Equation (46).

Our model also assumes a monodisperse distribution of particles, when true colloids (and especially environmental contaminants) are expected to be polydisperse. In the dilute limit $\phi \ll 1$, particle interactions can be neglected, and we expect that this model could still be easily applicable to a colloidal dispersion with a broad size distribution.

We also note that this theory is only concerned with the limit in which particle distribution is

fully developed, i.e., it becomes invariant in the streamwise direction when sufficiently far downstream. Naturally, the downstream lengthscale over which the particle distribution reaches this fully-developed state will also be key in designing separations driven by diffusiophoresis, since it would set a minimum design length to achieve the optimal water recovery given by (45). This lengthscale, obtained from balancing streamwise advection with cross-channel diffusiophoresis, can be estimated as $L_{\text{dev}} \sim W^2 U / \Gamma_p$, with U a typical velocity scale given by the streamwise flow rate. Further subtleties in the boundary layer analysis, such as the influence of spatially-varying shear in rectangular channels, can be found in reference 24.

Conclusions

We have developed a continuum theory to predict the maximum separation of a colloidal suspension driven by diffusiophoresis in a cross-channel electrolyte gradient. Three governing dimensionless parameters emerge from the theory: two Damköhler numbers Da_s and Da_i , given by Equation (21) and comparing the rates of dissociation kinetics to the diffusion of the solute and resulting ions, and a particle Péclet number Pe_p , given by Equation (16) and comparing diffusiophoretic migration to the Brownian diffusion of the particles. The model predicts four distinct regimes depending on the mechanism by which the delivered chemical permeates into the channel and on whether its dissociation kinetics are “strong” ($Da_s \gg Da_i$) or “weak” ($Da_s \ll Da_i$) compared to diffusion. All four regimes are governed by a single parameter δ measuring the width of the particle distribution, which displays distinct scalings in each regime as a function of Pe_p and, in certain regimes, also of Da_i and of a parameter ϵ that accounts for a small concentration at the chemical sink that may arise from imperfect transport through the channel walls. In addition, due to the asymmetry in the ion concentration and the boundary conditions at each wall, we distinguish between δ_+ at the source (for chemo-attracted particles) and δ_- at the sink (for chemo-repelled particles), which in general have different scalings. The expressions for the theory are summarized in Table 3, as well as the conditions of validity of the model. To conclude, we present microfluidic experiments using CO₂-driven diffusiophoresis that confirm the theoretical scaling in one of these four regimes, using polystyrene particles with three different surface functionalization and with diameters ranging from 0.08 μm to 1 μm.

Our analysis provides novel insights into the feasibility of diffusiophoresis as a method for colloid separation. First, it highlights that using a gas that strongly dissociates in water ($Da_i \ll Da_s$) leads to an unfavorable regime with low colloid separation, potentially unfeasible in applications. More importantly, it provides quantitative bounds for the

separation efficiency in all regimes, essential to assess its potential scalability and design separations driven by diffusiophoresis.

Acknowledgement We thank Suin Shim and J. Pedro de Souza for insightful discussions, and Mariko Storey-Matsutani for the assistance developing the experimental protocol. F.T-C. acknowledges support from a Distinguished Postdoctoral Fellowship from the Andlinger Center for Energy and the Environment. We acknowledge partial support from the National Science Foundation through grant CBET 2127563.

Supporting Information Available

Derivation of the leading-order particle profiles from the theory, detailed asymptotics for the ionic concentration profiles, and calibration of particle fluorescence intensity in the experiments.

References

- (1) Derjaguin, B. V.; Sidorenkov, G.; Zubashchenko, E.; Kiseleva, E. Kinetic Phenomena in the boundary layers of liquids. *Colloid J. USSR* **1947**, *9*, 335–347.
- (2) Derjaguin, B. V.; Dukhin, S. S.; Korotkova, A. A. Diffusiophoresis in electrolyte solutions and its role in the mechanism of the formation of films from caoutchouc latexes by the ionic deposition method. *Colloid J. USSR* **1961**, *23*, 53–58.
- (3) Prieve, D. C. Migration of a colloidal particle in a gradient of electrolyte concentration. *Adv. Colloid Interface Sci.* **1982**, *16*, 321–335.
- (4) Anderson, J. L.; Prieve, D. C. Diffusiophoresis: Migration of colloidal particles in gradients of solute concentration. *Sep. Purif. Methods* **1984**, *13*, 67–103.
- (5) Prieve, D. C.; Anderson, J. L.; Ebel, J. P.; Lowell, M. E. Motion of a particle generated by chemical gradients. Part 2. Electrolytes. *J. Fluid Mech.* **1984**, *148*, 247–269.
- (6) Prieve, D. C.; Roman, R. Diffusiophoresis of a rigid sphere through a viscous electrolyte solution. *J. Chem. Soc., Faraday Trans. 2* **1987**, *83*, 1287–1306.
- (7) Abécassis, B.; Cottin-Bizonne, C.; Ybert, C.; Ajdari, A.; Bocquet, L. Boosting migration of large particles by solute contrasts. *Nat. Mater.* **2008**, *7*, 785–789.
- (8) Shi, N.; Nery-Azevedo, R.; Abdel-Fattah, A. I.; Squires, T. M. Diffusiophoretic focusing of

Table 3: Summary of scaling relations for the nondimensional width δ of the particle distributions, for all four identified regimes, and conditions of validity of the theory.

Liquid source		Gas source		
	Chemo-attracted particles	Chemo-repelled particles	Chemo-attracted particles	
Strong dissociation	$\delta_+ = \frac{Pe_p^{-1}}{1 - \varepsilon^{1/\nu}}$	$\delta_- = \frac{\varepsilon^{1/\nu} Pe_p^{-1}}{1 - \varepsilon^{1/\nu}}$	$\delta_+ = 2^{\frac{2\nu-1}{2\nu}} Da_i^{-1/2} Pe_p^{-1/2}$	$\delta_- = 2^{\frac{2\nu-1}{2\nu}} Da_i^{-1/2} Pe_p^{-1/2}$
	$Pe_p \gg 1, Da_i \gg 1$	$Pe_p \gg 1, Da_i \gg 1$	$Pe_p \gg Da_i^{-1} \gg 1$	$Pe_p \gg Da_i^{-1} \gg 1$
Weak dissociation	$\delta_+ = \frac{\nu Pe_p^{-1}}{1 - \varepsilon}$	$\delta_- = \frac{\nu \varepsilon Pe_p^{-1}}{1 - \varepsilon}$	$\delta_+ = 2^{1/2} \nu^{1/4} Da_i^{-1/4} Pe_p^{-1/2}$	$\delta_- = 2^{1/2} \alpha^{\frac{1-\nu}{2}} Da_i^{\frac{-\nu}{3\nu-1}} Pe_p^{-\frac{1}{2}}$
	$Pe_p \gg 1, Da_i \gg 1$	$Pe_p \gg 1, Da_i \gg \varepsilon^{\frac{1-3\nu}{\nu}} \gg 1$	$Pe_p \gg Da_i^{1/2} \gg 1$	$Pe_p \gg 1, Da_i \gg 1$

suspended colloids. *Phys. Rev. Lett.* **2016**, *117*, 258001.

(9) Liu, H.; Pahlavan, A. A. Diffusioosmotic reversal of colloidal focusing direction in a microfluidic T-junction. *Phys. Rev. Lett.* **2025**, *134*, 098201.

(10) Sear, R. P.; Warren, P. B. Simple models for the trapping of charged particles and macromolecules by diffusiophoresis in salt gradients. *arXiv [cond-mat.soft]* **2025**,

(11) Banerjee, A.; Williams, I.; Azevedo, R. N.; Helgeson, M. E.; Squires, T. M. Soluto-inertial phenomena: Designing long-range, long-lasting, surface-specific interactions in suspensions. *Proc. Natl. Acad. Sci. U. S. A.* **2016**, *113*, 8612–8617.

(12) Banerjee, A.; Squires, T. M. Long-range, selective, on-demand suspension interactions: Combining and triggering soluto-inertial beacons. *Sci. Adv.* **2019**, *5*, eaax1893.

(13) Banerjee, A.; Vogus, D. R.; Squires, T. M. Design strategies for engineering soluto-inertial suspension interactions. *Phys. Rev. E* **2019**, *100*, 052603.

(14) Shin, S.; Um, E.; Sabass, B.; Ault, J. T.; Rahimi, M.; Warren, P. B.; Stone, H. A. Size-dependent control of colloid transport via solute gradients in dead-end channels. *Proc. Natl. Acad. Sci. U. S. A.* **2016**, *113*, 257–261.

(15) Doan, V. S.; Chun, S.; Feng, J.; Shin, S. Confinement-dependent diffusiophoretic transport of nanoparticles in collagen hydrogels. *Nano Lett.* **2021**, *21*, 7625–7630.

(16) Tan, H.; Banerjee, A.; Shi, N.; Tang, X.; Abdel-Fattah, A.; Squires, T. M. A two-step strategy for delivering particles to targets hidden within microfabricated porous media. *Sci. Adv.* **2021**, *7*, eabh0638.

(17) Akdeniz, B.; Wood, J. A.; Lammertink, R. G. H. Diffusiophoresis and diffusio-osmosis into a dead-end channel: Role of the concentration-dependence of zeta potential. *Langmuir* **2023**, *39*, 2322–2332.

(18) Shin, S.; Ault, J. T.; Feng, J.; Warren, P. B.; Stone, H. A. Low-cost zeta potentiometry using solute gradients. *Adv. Mater.* **2017**, *29*, 1701516.

(19) Rasmussen, M. K.; Pedersen, J. N.; Marie, R. Size and surface charge characterization of nanoparticles with a salt gradient. *Nat. Commun.* **2020**, *11*, 2337.

(20) Shim, S. Diffusiophoresis, diffusioosmosis, and microfluidics: Surface-flow-driven phenomena in the presence of flow. *Chem. Rev.* **2022**, *122*, 6986–7009.

(21) Ault, J. T.; Shin, S. Physicochemical hydrodynamics of particle diffusiophoresis driven by chemical gradients. *Annu. Rev. Fluid Mech.* **2025**, *57*, 227–255.

(22) Shin, S.; Shardt, O.; Warren, P. B.; Stone, H. A. Membraneless water filtration using CO₂. *Nat. Commun.* **2017**, *8*, 15181.

(23) Lee, H.; Kim, J.; Yang, J.; Seo, S. W.; Kim, S. J. Diffusiophoretic exclusion of colloidal particles for continuous water purification. *Lab Chip* **2018**, *18*, 1713–1724.

(24) Shim, S.; Baskaran, M.; Thai, E. H.; Stone, H. A. CO₂-Driven diffusiophoresis and water cleaning: similarity solutions for predicting the exclusion zone in a channel flow. *Lab Chip* **2021**, *21*, 3387–3400.

(25) Shin, S. Diffusiophoretic separation of colloids in microfluidic flows. *Phys. Fluids* **2020**, *32*, 101302.

(26) Shimokusu, T. J.; Maybruck, V. G.; Ault, J. T.; Shin, S. Colloid separation by CO₂-induced diffusiophoresis. *Langmuir* **2020**, *36*, 7032–7038.

(27) Chakra, A.; Puijk, C.; Vladisavljević, G. T.; Cottin-Bizonne, C.; Pirat, C.; Bolognesi, G. Surface chemistry-based continuous separation of colloidal particles via diffusiophoresis and diffusioosmosis. *J. Colloid Interface Sci.* **2025**, *693*, 137577.

(28) Belfort, G.; Davis, R. H.; Zydny, A. L. The behavior of suspensions and macromolecular solutions in crossflow microfiltration. *J. Memb. Sci.* **1994**, *96*, 1–58.

(29) Tang, C. Y.; Chong, T. H.; Fane, A. G. Colloidal interactions and fouling of NF and RO membranes: a review. *Adv. Colloid Interface Sci.* **2011**, *164*, 126–143.

(30) Rochman, C. M. Microplastics research—from sink to source. *Science* **2018**, *360*, 28–29.

(31) Hale, R. C.; Seeley, M. E.; La Guardia, M. J.; Mai, L.; Zeng, E. Y. A global perspective on microplastics. *J. Geophys. Res. Oceans* **2020**, *125*, e2018JC014719.

(32) Qian, N.; Gao, X.; Lang, X.; Deng, H.; Bratu, T. M.; Chen, Q.; Stapleton, P.; Yan, B.; Min, W. Rapid single-particle chemical imaging of nanoplastics by SRS microscopy. *Proc. Natl. Acad. Sci. U. S. A.* **2024**, *121*, e2300582121.

(33) Newman, J.; Thomas-Alyea, K. E. *Electrochemical Systems*; John Wiley & Sons, 2012.

(34) Paustian, J. S.; Azevedo, R. N.; Lundin, S.-T. B.; Gilkey, M. J.; Squires, T. M. Microfluidic microdialysis: spatiotemporal control over solution microenvironments using integrated hydrogel membrane microwindows. *Phys. Rev. X* **2013**, *3*, 041010.

(35) Shim, S.; Stone, H. A. CO₂-leakage-driven diffusiophoresis causes spontaneous accumulation of charged materials in channel flow. *Proc. Natl. Acad. Sci. U. S. A.* **2020**,

(36) Shim, S.; Khodaparast, S.; Lai, C.-Y.; Yan, J.; Ault, J. T.; Rallabandi, B.; Shardt, O.; Stone, H. A. CO₂-Driven diffusiophoresis for maintaining a bacteria-free surface. *Soft Matter* **2021**, *17*, 2568–2576.

(37) Paustian, J. S.; Angulo, C. D.; Nery-Azevedo, R.; Shi, N.; Abdel-Fattah, A. I.; Squires, T. M. Direct measurements of colloidal solvophoresis under imposed solvent and solute gradients. *Langmuir* **2015**, *31*, 4402–4410.

(38) Nery-Azevedo, R.; Banerjee, A.; Squires, T. M. Diffusiophoresis in ionic surfactant gradients. *Langmuir* **2017**, *33*, 9694–9702.

(39) Shah, P. R.; Tan, H.; Taylor, D.; Tang, X.; Shi, N.; Mashat, A.; Abdel-Fattah, A.; Squires, T. M. Temperature dependence of diffusiophoresis via a novel microfluidic approach. *Lab Chip* **2022**, *22*, 1980–1988.

(40) Wijmans, J. G.; Baker, R. W. The solution-diffusion model: a review. *J. Memb. Sci.* **1995**, *107*, 1–21.

(41) Gupta, A.; Shim, S.; Stone, H. A. Diffusiophoresis: from dilute to concentrated electrolytes. *Soft Matter* **2020**, *16*, 6975–6984.

(42) Hinch, E. J. *Perturbation methods*; Cambridge University Press: Cambridge, England, 1991.

(43) Bender, C. M.; Orszag, S. A. *Advanced mathematical methods for scientists and engineers I: Asymptotic methods and perturbation theory*; Springer, New York, NY, 1999.

(44) Leal, L. G. *Advanced transport phenomena: Fluid mechanics and convective transport processes*; Cambridge University Press, 2007.

(45) Alkhadra, M. A.; Su, X.; Suss, M. E.; Tian, H.; Guyes, E. N.; Shocron, A. N.; Conforti, K. M.; de Souza, J. P.; Kim, N.; Tedesco, M.; Khoiruddin, K.; Wenten, I. G.; Santiago, J. G.; Hatton, T. A.; Bazant, M. Z. Electrochemical methods for water purification, ion separations, and energy conversion. *Chem. Rev.* **2022**, *122*, 13547–13635.

(46) Merkel, T. C.; Bondar, V. I.; Nagai, K.; Freeman, B. D.; Pinna, I. Gas sorption, diffusion, and permeation in poly(dimethylsiloxane). *J. Polym. Sci. B Polym. Phys.* **2000**, *38*, 415–434.

(47) Jolly, W. L. *Modern inorganic chemistry*, 2nd ed.; McGraw-Hill: New York, NY, 1991.

(48) Guazzelli, E.; Morris, J. F. *A physical introduction to suspension dynamics*; Cambridge University Press: Cambridge, England, 2012.

- (49) Shim, S.; Nunes, J. K.; Chen, G.; Stone, H. A. Diffusiophoresis in the presence of a pH gradient. *Phys. Rev. Fluids* **2022**, *7*, 110513.
- (50) Kern, D. M. The hydration of carbon dioxide. *J. Chem. Educ.* **1960**, *37*, 14.

Supporting Information:

Upper bounds on the separation efficiency of diffusiophoresis

Fernando Temprano-Coleto,^{†,‡} Jeongmin Kim,[†] Marcel M. Louis,[†] and Howard A. Stone^{*,†}

[†] Department of Mechanical and Aerospace Engineering, Princeton University, Princeton, NJ 08544, USA

[‡] Andlinger Center for Energy and the Environment, Princeton University, Princeton, NJ 08544, USA

E-mail: hastone@princeton.edu

Derivation of the leading-order particle profiles

Liquid sources

We start by combining the exact solution for the particle concentrations [Equation (19) in the main text] with the Taylor expansions for c_i for liquid sources [Equation (28) in the main text]. After factoring out $c_i(0)$ from the numerator and denominator, and noting that the derivative at walls is negative at the source ($dc_i/dy_+ < 0$ at $y_+ = 0$) and positive at the sink ($dc_i/dy_- > 0$ at $y_- = 0$), we obtain

$$n_{\pm} = \frac{\left[1 \mp \frac{1}{c_i(0)} \left| \frac{dc_i}{dy_{\pm}}(0) \right| y_{\pm} + O(y_{\pm}^2) \right]^{\pm Pe_p}}{\int_0^1 \left[1 \mp \frac{1}{c_i(0)} \left| \frac{dc_i}{dy_{\pm}}(0) \right| y_{\pm} + O(y_{\pm}^2) \right]^{\pm Pe_p} dy_{\pm}}. \quad (\text{S1})$$

We then seek to find approximations for this expression at distances sufficiently close to the walls, where y_{\pm} is sufficiently small. To that end, we define $y_{\pm} := \delta_{\pm} \xi_{\pm}$ as a rescaled wall coordinate, such that $\xi_{\pm} = O(1)$ wherever $y_{\pm} = O(\delta_{\pm})$, and with δ_{\pm} the (small) boundary layer thickness. This leads to

$$n_{\pm} = \frac{\left[1 \mp \frac{1}{c_i(0)} \left| \frac{dc_i}{dy_{\pm}}(0) \right| \delta_{\pm} \xi_{\pm} + O(\xi_{\pm}^2) \right]^{\pm Pe_p}}{\int_0^1 \left[1 \mp \frac{1}{c_i(0)} \left| \frac{dc_i}{dy_{\pm}}(0) \right| \delta_{\pm} \xi_{\pm} + O(\xi_{\pm}^2) \right]^{\pm Pe_p} dy_{\pm}}. \quad (\text{S2})$$

Since we expect a large absolute value of the exponent $Pe_p \gg 1$, we expect the terms of the expansion to be small if the boundary layer thickness is

$$\delta_{\pm} = \frac{c_i(0)}{\left| \frac{dc_i}{dy_{\pm}}(0) \right|} Pe_p^{-1}, \quad (S3)$$

such that

$$n_{\pm} = \frac{\left[1 \mp \frac{\xi_{\pm}}{Pe_p} + O(Pe_p^{-2}) \right]^{\pm Pe_p}}{\delta_{\pm} \int_0^{1/\delta_{\pm}} \left[1 \mp \frac{\xi_{\pm}}{Pe_p} + O(Pe_p^{-2}) \right]^{\pm Pe_p} d\xi_{\pm}}. \quad (S4)$$

Since the Péclet number is large, we can then invoke that $\left[1 \mp \frac{\xi_{\pm}}{Pe_p} + O(Pe_p^{-2}) \right]^{\pm Pe_p} = e^{-\xi_{\pm}} [1 + O(Pe_p^{-1})]$ and, after integrating, obtain

$$n_{\pm} = \frac{e^{-\xi_{\pm}}}{\delta_{\pm} (1 - e^{-1/\delta_{\pm}})} + o(\delta_{\pm}^{-1}), \quad (S5)$$

which, after neglecting exponentially small terms and changing variables back to y_{\pm} , results in

$$n_{\pm} = \frac{e^{-y_{\pm}/\delta_{\pm}}}{\delta_{\pm}} + o(\delta_{\pm}^{-1}), \quad (S6)$$

whose leading-order term $n_{\pm}^{(0)}$ is given by Equation (30a) in the main text.

Gas sources

We can follow an analogous procedure combining the exact solution for the particles [Equation (19) in the main text] with the Taylor expansions for c_i for gas sources [Equation (29) in the main text]. After factoring out $c_i(0)$ from the numerator and denominator, and noting that the second derivative at walls is negative at the source ($d^2 c_i / dy_{+}^2 < 0$ at $y_{+} = 0$) and positive at the sink ($d^2 c_i / dy_{-}^2 > 0$ at $y_{-} = 0$), we obtain

$$n_{\pm} = \frac{\left[1 \mp \frac{1}{c_i(0)} \left| \frac{d^2 c_i}{dy_{\pm}^2}(0) \right| \frac{y_{\pm}^2}{2} + O(y_{\pm}^3) \right]^{\pm Pe_p}}{\int_0^1 \left[1 \mp \frac{1}{c_i(0)} \left| \frac{d^2 c_i}{dy_{\pm}^2}(0) \right| \frac{y_{\pm}^2}{2} + O(y_{\pm}^3) \right]^{\pm Pe_p} dy_{\pm}}. \quad (S7)$$

Defining $y_{\pm} := \delta_{\pm} \xi_{\pm}$ with a boundary layer thickness δ_{\pm} such that

$$\delta_{\pm} = \left[\frac{2c_i(0)}{\left| \frac{d^2 c_i}{dy_{\pm}^2}(0) \right|} \right]^{1/2} Pe_p^{-1/2}, \quad (S8)$$

we obtain

$$n_{\pm} = \frac{\left[1 \mp \frac{\xi_{\pm}^2}{Pe_p} + O(Pe_p^{-2}) \right]^{\pm Pe_p}}{\delta_{\pm} \int_0^{1/\delta_{\pm}} \left[1 \mp \frac{\xi_{\pm}^2}{Pe_p} + O(Pe_p^{-2}) \right]^{\pm Pe_p} d\xi_{\pm}}. \quad (S9)$$

After noting $\left[1 \mp \frac{\xi_{\pm}^2}{Pe_p} + O(Pe_p^{-2}) \right]^{\pm Pe_p} = e^{-\xi_{\pm}^2} [1 + O(Pe_p^{-1})]$, integrating, and neglecting exponentially small terms, we obtain

$$n_{\pm} = \frac{2e^{-\left(\frac{y_{\pm}}{\delta_{\pm}}\right)^2}}{\delta_{\pm} \sqrt{\pi}} + o(\delta_{\pm}^{-1}), \quad (S10)$$

whose leading-order term $n_{\pm}^{(0)}$ is given by Equation (30b) of the main text.

Detailed asymptotics for the ionic concentration profiles

Strong dissociation - Gas sources

Inserting the expansion $c_i = c_i^{(0)} + Da_i c_i^{(1)} + O(Da_i^2)$ into Equation (23) of the main text, we obtain, at leading order,

$$\frac{d^4 c_i^{(0)}}{dy^4} = Da_s \frac{d^2 c_i^{(0)}}{dy^2}, \quad (S11)$$

which has a solution

$$c_i^{(0)} = A + B y + C e^{-\sqrt{Da_s} y} + D e^{\sqrt{Da_s} y}, \quad (S12)$$

and with A, B, C, D constants. The boundary conditions given by (25) in the main text result in

$$\frac{d^2 c_i^{(0)}}{dy^2}(0) = \frac{d^2 c_i^{(0)}}{dy^2}(1) = \frac{dc_i^{(0)}}{dy}(0) = \frac{dc_i^{(0)}}{dy}(1) = 0 \quad (S13)$$

at leading order, which give $B = C = D = 0$ and $c_i^{(0)} = A$, with A undetermined.

At first order in Da_i , the governing equation is the same as in the zeroth-order case, i.e.

$$\frac{d^4 c_i^{(1)}}{dy^4} = Da_s \frac{d^2 c_i^{(1)}}{dy^2}, \quad (S14)$$

with boundary conditions

$$\frac{d^2 c_i^{(1)}}{dy^2}(0) = \left(c_i^{(0)}\right)^\nu - 1 = A^\nu - 1 \quad \text{at } y = 0, \quad (S15a)$$

$$\frac{d^2 c_i^{(1)}}{dy^2}(1) = \left(c_i^{(0)}\right)^\nu = A^\nu \quad \text{at } y = 1, \quad (S15b)$$

$$\frac{dc_i^{(1)}}{dy}(0) = 0 \quad \text{at } y = 0, \quad (S15c)$$

$$\frac{dc_i^{(1)}}{dy}(1) = 0 \quad \text{at } y = 1. \quad (S15d)$$

The general solution of (S14) is $c_i^{(1)} = E + Fy + Ge^{-\sqrt{Da_s}y} + He^{\sqrt{Da_s}y}$, leaving five constants (A , E , F , G , and H) to be determined with only four boundary conditions (S15). However, an additional solvability condition can be determined integrating (S14) and imposing the no-flux conditions (S15c) and (S15d),

$$\begin{aligned} \int_0^1 \frac{d^4 c_i^{(1)}}{dy^4} dy &= Da_s \int_0^1 \frac{d^2 c_i^{(1)}}{dy^2} dy, \\ \frac{d^3 c_i^{(1)}}{dy^3}(1) - \frac{d^3 c_i^{(1)}}{dy^3}(0) &= Da_s \left[\frac{dc_i^{(1)}}{dy}(1) - \frac{dc_i^{(1)}}{dy}(0) \right] = 0, \\ \frac{d^3 c_i^{(1)}}{dy^3}(1) &= \frac{d^3 c_i^{(1)}}{dy^3}(0). \end{aligned} \quad (S16)$$

After solving for the constants, we obtain $A = 2^{-1/\nu}$ and the solutions $c_i^{(0)}$ and $c_i^{(1)}$ given by Equations (36) in the main text.

Weak dissociation - Liquid sources

Inserting the expansion $c_i = c_i^{(0)} + Da_i^{-1}c_i^{(1)} + O(Da_i^{-2})$ into Equation (23) of the main text, we obtain

$$\frac{d^2}{dy^2} \left[\left(c_i^{(0)}\right)^\nu \right] = 0, \quad (S17a)$$

$$\frac{d^2}{dy^2} \left[\nu \left(c_i^{(0)}\right)^{\nu-1} c_i^{(1)} \right] = \frac{d^4 c_i^{(0)}}{dy^4} - Da_s \frac{d^2 c_i^{(0)}}{dy^2}, \quad (S17b)$$

at zeroth and first order, respectively, which have solutions given by

$$c_i^{(0)} = [A + By]^{1/\nu}, \quad (\text{S18a})$$

$$c_i^{(1)} = -\frac{B^2(\nu - 1)}{\nu^3} [A + By]^{\frac{2-3\nu}{\nu}} - \frac{Da_s}{\nu} [A + By]^{\frac{2-\nu}{\nu}} + \frac{C + Dy}{\nu} [A + By]^{\frac{1-\nu}{\nu}}, \quad (\text{S18b})$$

However, these are only an “outer” solutions since they cannot satisfy all four boundary conditions given by (24) at each order simultaneously.

To find the solution close to the domain boundaries, we first introduce a rescaled “inner” coordinate y_B near the (bottom) $y = 0$ wall, such that

$$y_B = Da_i^m y, \quad (\text{S19})$$

and introduce it into the governing equation (23) to obtain the inner equation

$$\frac{d^4 c_{iB}}{dy_B^4} = Da_i^{1-2m} \frac{d^2}{dy_B^2} [(c_{iB})^\nu] + Da_s Da_i^{-2m} \frac{d^2 c_{iB}}{dy_B^2}, \quad (\text{S20})$$

where we have denoted the inner solution as c_{iB} for notational convenience. The value $m = 1/2$ is required to retain a meaningful dominant balance of terms, which leads to

$$\frac{d^4 c_{iB}}{dy_B^4} = \frac{d^2}{dy_B^2} [(c_{iB})^\nu] + Da_s Da_i^{-1} \frac{d^2 c_{iB}}{dy_B^2}, \quad (\text{S21})$$

which must be solved order by order imposing the boundary conditions at $y_B = 0$ and matching to the outer solution as $y_B \rightarrow \infty$. To find out the terms in the matching, we expand the outer solution in the inner coordinate y_B as

$$\begin{aligned} c_i(y_B) &= c_i^{(0)}(y_B) + Da_i^{-1} c_i^{(1)}(y_B) + O(Da_i^{-2}) = \\ &= [A + Da_i^{-1/2} B y_B]^{1/\nu} + Da_i^{-1} c_i^{(1)}(y_B) + O(Da_i^{-2}) = \\ &= A^{1/\nu} + Da_i^{-1/2} \frac{A^{\frac{1-\nu}{\nu}} B}{\nu} y_B + Da_i^{-1} \left[-\frac{A^{\frac{1-2\nu}{\nu}} B^2(\nu - 1)}{2\nu^2} y_B^2 + c_i^{(1)}(y_B = 0) \right] + O(Da_i^{-3/2}). \end{aligned} \quad (\text{S22})$$

We then pose an expansion of the inner solution $c_{iB} = c_{iB}^{(0)} + Da_i^{-1/2} c_{iB}^{(1)} + Da_i^{-1} c_{iB}^{(2)} + O(Da_i^{-3/2})$ and insert it in the inner equation (S21) and in the boundary conditions to obtain the inner problem at each order.

At zeroth order, we have

$$\frac{d^4 c_{iB}^{(0)}}{dy_B^4} = \frac{d^2}{dy_B^2} \left[\left(c_{iB}^{(0)} \right)^\nu \right], \quad (S23a)$$

$$c_{iB}^{(0)} = 1 \text{ at } y_B = 0, \quad (S23b)$$

$$\frac{d^2 c_{iB}^{(0)}}{dy_B^2} = 0 \text{ at } y_B = 0, \quad (S23c)$$

$$c_{iB}^{(0)} \rightarrow A^{1/\nu} \text{ as } y_B \rightarrow \infty, \quad (S23d)$$

which requires the constant to be $A = 1$ and results in $c_{iB}^{(0)} = 1$.

At order $Da_i^{-1/2}$, we find

$$\frac{d^4 c_{iB}^{(1)}}{dy_B^4} = \nu \frac{d^2 c_{iB}^{(1)}}{dy_B^2}, \quad (S24a)$$

$$c_{iB}^{(1)} = 0 \text{ at } y_B = 0, \quad (S24b)$$

$$\frac{d^2 c_{iB}^{(1)}}{dy_B^2} = 0 \text{ at } y_B = 0, \quad (S24c)$$

$$c_{iB}^{(1)} \rightarrow \frac{B}{\nu} y_B \text{ as } y_B \rightarrow \infty, \quad (S24d)$$

which has solution $c_{iB}^{(1)} = \frac{B}{\nu} y_B$.

At order Da_i^{-1} , we find

$$\frac{d^4 c_{iB}^{(2)}}{dy_B^4} = \nu \frac{d^2}{dy_B^2} \left[\frac{(\nu-1)B^2}{2\nu^2} y_B^2 + c_{iB}^{(2)} \right], \quad (S25a)$$

$$c_{iB}^{(2)} = 0 \text{ at } y_B = 0, \quad (S25b)$$

$$\frac{d^2 c_{iB}^{(2)}}{dy_B^2} = 0 \text{ at } y_B = 0, \quad (S25c)$$

$$c_{iB}^{(2)} \rightarrow -\frac{(\nu-1)B^2}{2\nu^2} y_B^2 \text{ as } y_B \rightarrow \infty, \quad (S25d)$$

which has solution $c_{iB}^{(2)} = \frac{(\nu-1)B^2}{\nu^3} \left[e^{-\sqrt{\nu}y_B} - \frac{\nu}{2} y_B^2 - 1 \right]$.

We can then proceed analogously with the boundary-layer analysis of the (top) $y = 1$ wall. Introducing a rescaled “inner” coordinate y_T such that

$$y_T = Da_i^{1/2} (1 - y), \quad (S26)$$

and plugging it into Equation (23) of the main text, we obtain the inner equation

$$\frac{d^4 c_{iT}}{dy_T^4} = \frac{d^2}{dy_T^2} [(c_{iT})^\nu] + Da_s Da_i^{-1} \frac{d^2 c_{iT}}{dy_T^2}. \quad (\text{S27})$$

Expanding the outer solution in the inner coordinate y_T , we arrive at

$$\begin{aligned} c_i(y_T) &= c_i^{(0)}(y_T) + Da_i^{-1} c_i^{(1)}(y_T) + O(Da_i^{-2}) = \\ &= [(1 + B) - Da_i^{-1/2} B y_T]^{1/\nu} + Da_i^{-1} c_i^{(1)}(y_T) + O(Da_i^{-2}) = \\ &= (1 + B)^{1/\nu} - Da_i^{-1/2} \frac{B(1 + B)^{\frac{1-\nu}{\nu}}}{\nu} y_T + \\ &\quad + Da_i^{-1} \left[-\frac{(\nu - 1)B^2(1 + B)^{\frac{1-2\nu}{\nu}}}{2\nu^2} y_T^2 + c_i^{(1)}(y_T = 0) \right] + O(Da_i^{-3/2}), \end{aligned} \quad (\text{S28})$$

where we have already used $A = 1$ obtained from the matching conditions at the bottom $y = 0$ boundary.

Then, we insert an expansion of the inner solution $c_{iT} = c_{iT}^{(0)} + Da_i^{-1/2} c_{iT}^{(1)} + Da_i^{-1} c_{iT}^{(2)} + O(Da_i^{-3/2})$ in the inner equation (S27) and in the boundary conditions to obtain the inner problem at each order.

At zeroth order, we have

$$\frac{d^4 c_{iT}^{(0)}}{dy_T^4} = \frac{d^2}{dy_T^2} \left[\left(c_{iT}^{(0)} \right)^\nu \right], \quad (\text{S29a})$$

$$c_{iT}^{(0)} = \varepsilon^{1/\nu} \text{ at } y_T = 0, \quad (\text{S29b})$$

$$\frac{d^2 c_{iT}^{(0)}}{dy_T^2} = 0 \text{ at } y_T = 0, \quad (\text{S29c})$$

$$c_{iT}^{(0)} \rightarrow (1 + B)^{1/\nu} \text{ as } y_T \rightarrow \infty, \quad (\text{S29d})$$

which requires the constant to be $B = \varepsilon - 1$ and results in $c_{iT}^{(0)} = \varepsilon^{1/\nu}$.

At order $Da_i^{-1/2}$, we find

$$\frac{d^4 c_{iT}^{(1)}}{dy_T^4} = \nu \varepsilon^{\frac{\nu-1}{\nu}} \frac{d^2 c_{iT}^{(1)}}{dy_T^2}, \quad (\text{S30a})$$

$$c_{iT}^{(1)} = 0 \text{ at } y_T = 0, \quad (\text{S30b})$$

$$\frac{d^2 c_{iT}^{(1)}}{dy_T^2} = 0 \text{ at } y_T = 0, \quad (\text{S30c})$$

$$c_{iT}^{(1)} \rightarrow \frac{(1 - \varepsilon) \varepsilon^{\frac{1-\nu}{\nu}}}{\nu} y_T \text{ as } y_T \rightarrow \infty, \quad (\text{S30d})$$

with solution $c_{iT}^{(1)} = \frac{(1-\varepsilon)\varepsilon^{\frac{1-\nu}{\nu}}}{\nu} y_T$.

At order Da_i^{-1} , we find

$$\frac{d^4 c_{iT}^{(1)}}{dy_T^4} = \nu \varepsilon^{\frac{\nu-1}{\nu}} \frac{d^2}{dy_T^2} \left[\frac{(\nu-1)(1-\varepsilon)^2 \varepsilon^{\frac{1-2\nu}{\nu}}}{2\nu^2} y_T^2 + c_{iT}^{(2)} \right], \quad (\text{S31a})$$

$$c_{iT}^{(2)} = 0 \text{ at } y_T = 0, \quad (\text{S31b})$$

$$\frac{d^2 c_{iT}^{(2)}}{dy_T^2} = 0 \text{ at } y_T = 0, \quad (\text{S31c})$$

$$c_{iT}^{(2)} \rightarrow -\frac{(\nu-1)(1-\varepsilon)^2 \varepsilon^{\frac{1-2\nu}{\nu}}}{2\nu^2} y_T^2 \text{ as } y_T \rightarrow \infty, \quad (\text{S31d})$$

which has solution $c_{iT}^{(2)} = \frac{(\nu-1)(1-\varepsilon)^2 \varepsilon^{\frac{2-3\nu}{\nu}}}{\nu^3} \left[e^{-\sqrt{\nu}\varepsilon^{\frac{\nu-1}{2\nu}} y_T} - \frac{\nu \varepsilon^{\frac{\nu-1}{\nu}}}{2} y_T^2 - 1 \right]$.

In summary, the solutions near the bottom and top walls can then be expressed as

$$c_{iB} = 1 - Da_i^{-1/2} \frac{(1-\varepsilon)}{\nu} y_B + Da_i^{-1} \frac{(\nu-1)(1-\varepsilon)^2}{\nu^3} \left[e^{-\sqrt{\nu}y_B} - \frac{\nu}{2} y_B^2 - 1 \right] + O(Da_i^{-3/2}), \quad (\text{S32a})$$

$$c_{iT} = \varepsilon^{1/\nu} - Da_i^{-1/2} \frac{(1-\varepsilon)\varepsilon^{\frac{1-\nu}{\nu}}}{\nu} y_T + Da_i^{-1} \frac{(\nu-1)(1-\varepsilon)^2 \varepsilon^{\frac{2-3\nu}{\nu}}}{\nu^3} \left[e^{-\sqrt{\nu}\varepsilon^{\frac{\nu-1}{2\nu}} y_T} - \frac{\nu \varepsilon^{\frac{\nu-1}{\nu}}}{2} y_T^2 - 1 \right] + O(Da_i^{-3/2}), \quad (\text{S32b})$$

which can be re-expressed in terms of the outer variables $y_+ = Da_i^{1/2} y_B$ and $y_- = Da_i^{1/2} y_T$ and then expanded up to linear order to obtain

$$c_i \approx 1 - \frac{(1-\varepsilon)}{\nu} \left[1 + Da_i^{-1/2} \frac{(\nu-1)(1-\varepsilon)}{\nu^{3/2}} \right] y_+ \quad \text{at the source,} \quad (\text{S33a})$$

$$c_i \approx \varepsilon^{1/\nu} + \frac{(1-\varepsilon)\varepsilon^{\frac{1-\nu}{\nu}}}{\nu} \left[1 - Da_i^{-1/2} \frac{(\nu-1)(1-\varepsilon)\varepsilon^{\frac{1-3\nu}{2\nu}}}{\nu^{3/2}} \right] y_- \quad \text{at the sink.} \quad (\text{S33b})$$

After neglecting terms of order $Da_i^{-1/2}$, the above expressions (S33) simplify into Equations (39) in the main text. It is worth remarking that, since $\nu > 1$ and $0 < \varepsilon < 1$, the $O(Da_i^{-1/2})$ term in (S33a) can always be neglected for sufficiently large $Da_i \gg 1$. However, the expression $\varepsilon^{\frac{1-3\nu}{2\nu}}$ could become large if $\varepsilon \ll 1$, potentially compensating the small $Da_i^{-1/2}$ and invalidating the asymptotic expansion. This breakdown of the theory stems from the implicit assumption that $\varepsilon = O(1)$. Since a more careful analysis for a small $\varepsilon \ll 1$ would be out of the scope of this paper, we simply remark that the theory will be valid as long as

$$Da_i \gg \frac{(\nu-1)^2}{\nu^3} (1-\varepsilon)^2 \varepsilon^{\frac{1-3\nu}{\nu}}, \quad (\text{S34})$$

under which the $O(Da_i^{-1/2})$ term in (S33b) can clearly be safely neglected.

Weak dissociation - Gas sources

In the case of gas sources, the only difference with respect to the liquid sources is the boundary conditions. Therefore, we also pose an expansion $c_i = c_i^{(0)} + Da_i^{-1}c_i^{(1)} + O(Da_i^{-2})$, insert it in Equation (23) of the main text, and obtain the same outer solutions

$$c_i^{(0)} = [A + By]^{1/\nu}, \quad (\text{S35a})$$

$$c_i^{(1)} = -\frac{B^2(\nu-1)}{\nu^3} [A + By]^{\frac{2-3\nu}{\nu}} - \frac{Da_s}{\nu} [A + By]^{\frac{2-\nu}{\nu}} + \frac{C + Dy}{\nu} [A + By]^{\frac{1-\nu}{\nu}}, \quad (\text{S35b})$$

at zeroth and first order, respectively. Note that these are identical to the outer solution for the case of a liquid source (S18).

To find the inner solution close to the bottom $y = 0$ boundary, we introduce the same rescaled “inner” coordinate y_B near the (bottom) $y = 0$ wall as in the case for liquid sources, such that

$$y_B = Da_i^{1/2}y, \quad (\text{S36})$$

which, once introduced in the governing equation (23), leads to a hierarchy of inner problems analogous to those of the case with liquid sources (S23) and (S24), with the same matching conditions but with different boundary conditions at the bottom wall $y_B = 0$.

At zeroth order, the inner problem is

$$\frac{d^4 c_{iB}^{(0)}}{dy_B^4} = \frac{d^2}{dy_B^2} \left[\left(c_{iB}^{(0)} \right)^\nu \right], \quad (\text{S37a})$$

$$\left(c_{iB}^{(0)} \right)^\nu - \frac{d^2 c_{iB}^{(0)}}{dy_B^2} = 1 \text{ at } y_B = 0, \quad (\text{S37b})$$

$$\frac{dc_{iB}^{(0)}}{dy_B} = 0 \text{ at } y_B = 0, \quad (\text{S37c})$$

$$c_{iB}^{(0)} \rightarrow A^{1/\nu} \text{ as } y_B \rightarrow \infty, \quad (\text{S37d})$$

which leads to $A = 1$ and to a solution $c_{iB}^{(0)} = 1$.

At order $Da_i^{-1/2}$, the inner problem is

$$\frac{d^4 c_{iB}^{(1)}}{dy_B^4} = \nu \frac{d^2 c_{iB}^{(1)}}{dy_B^2}, \quad (\text{S38a})$$

$$c_{iB}^{(1)} - \frac{d^2 c_{iB}^{(1)}}{dy_B^2} = 0 \text{ at } y_B = 0, \quad (\text{S38b})$$

$$\frac{d^1 c_{iB}^{(1)}}{dy_B^1} = 0 \text{ at } y_B = 0, \quad (\text{S38c})$$

$$c_{iB}^{(1)} \rightarrow \frac{B}{\nu} y_B \text{ as } y_B \rightarrow \infty, \quad (\text{S38d})$$

which has solution $c_{iB}^{(1)} = \frac{B}{\nu} \left[y_B + \frac{e^{-\sqrt{\nu} y_B}}{\nu^{1/2}} \right]$.

To find the inner solution close to the top $y = 1$ boundary, we need a different boundary layer rescaling, since a naive $y_T = Da_i^{1/2}(1 - y)$ fails to produce a consistent leading-order inner problem. The reason for this is that, unlike the case of a liquid source where $c_i(y = 1) \rightarrow \varepsilon$ as $Da_i \rightarrow \infty$, for a gas source we have that $c_i(y = 1) \rightarrow 0$ as $Da_i \rightarrow \infty$, and therefore $c_i(y = 1)$ can get arbitrarily small and must also be rescaled by a small parameter to arrive at a consistent inner problem. We therefore pose a scaling

$$y_T = Da_i^m(1 - y), \quad (\text{S39a})$$

$$c_{iT} = Da_i^n c_i, \quad (\text{S39b})$$

which, introduced in Equation (23) of the main text, leads to

$$\frac{d^4 c_{iT}}{dy_T^4} = Da_i^{1-2m-(\nu-1)n} \frac{d^2}{dy_T^2} [(c_{iT})^\nu] + Da_s Da_i^{-2m} \frac{d^2 c_{iT}}{dy_T^2}. \quad (\text{S40})$$

Similarly, this rescaling turns the boundary conditions (25b) and (25c) of the main text into

$$Da_i^{1-2m-(\nu-1)n} c_{iT}^\nu - \frac{d^2 c_{iT}}{dy_T^2} = 0, \quad (\text{S41a})$$

$$\frac{dc_{iT}}{dy_T} = 0. \quad (\text{S41b})$$

We therefore set

$$n = \frac{1-2m}{\nu-1} \quad (\text{S42})$$

to achieve a meaningful dominant balance. We can then determine the value of m by examining the matching condition: expressing the outer solution in terms of the inner variable y_T and noting that $A = 1$ from the

previous analysis, we obtain

$$c_i(y_T) = [(1 + B) - Da_i^{-m} B y_T]^{1/n} + O(Da_i^{-1}). \quad (\text{S43})$$

The matching condition dictates that, if $B \neq 0$, the inner solution must satisfy $Da_i^{-n} c_{iT} \rightarrow (1 + B)^{1/\nu}$ as $y_T \rightarrow \infty$ at leading order. This condition can be satisfied with $n = 0$, which reverts to $m = 1/2$ and the naive scaling $y_T = Da_i^{1/2}(1 - y)$, and to an leading order problem given by

$$\frac{d^4 c_{iT}^{(0)}}{dy_T^4} = \frac{d^2}{dy_T^2} \left[\left(c_{iT}^{(0)} \right)^\nu \right], \quad (\text{S44a})$$

$$c_{iT}^\nu - \frac{d^2 c_{iT}}{dy_T^2} = 0 \text{ at } y_T = 0, \quad (\text{S44b})$$

$$\frac{dc_{iT}^{(0)}}{dy_T} = 0 \text{ at } y_T = 0, \quad (\text{S44c})$$

$$c_{iT}^{(0)} \rightarrow (1 + B)^{1/\nu} \text{ as } y_T \rightarrow \infty, \quad (\text{S44d})$$

which only admits a solution if $B = -1$, which contradicts our prior assumption. The only option left is then that $B = -1$ but $n \neq 0$, in which case the outer solution can be expanded as

$$c_i(y_T) = Da_i^{-m/\nu} y_T^{1/\nu} + O(Da_i^{-1}). \quad (\text{S45})$$

The leading-order matching condition at leading order is then $Da_i^{-n} c_{iT} \rightarrow Da_i^{-m/\nu} y_T^{1/\nu}$ as $y_T \rightarrow \infty$, which requires $m = \nu n$. In combination with the previous condition of $n = (1 - 2m)/(\nu - 1)$, this leads to

$$m = \frac{\nu}{3\nu - 1}, \quad (\text{S46a})$$

$$n = \frac{1}{3\nu - 1}, \quad (\text{S46b})$$

with values tabulated in Table S1.

Table S1: Values of the exponents m and n in Equation (S46) for different values of ν .

ν	2	3	4	5
m	2/5	3/8	4/11	5/14
n	1/5	1/8	1/11	1/14

With these exponents, we arrive at the zeroth-order inner problem

$$\frac{d^4 c_{iT}^{(0)}}{dy_T^4} = \frac{d^2}{dy_T^2} \left[\left(c_{iT}^{(0)} \right)^\nu \right], \quad (S47a)$$

$$c_{iT}^\nu - \frac{d^2 c_{iT}}{dy_T^2} = 0 \text{ at } y_T = 0, \quad (S47b)$$

$$\frac{dc_{iT}^{(0)}}{dy_T} = 0 \text{ at } y_T = 0, \quad (S47c)$$

$$c_{iT}^{(0)} \rightarrow y_T^{1/\nu} \text{ as } y_T \rightarrow \infty, \quad (S47d)$$

which can be integrated twice to yield

$$\frac{d^2 c_{iT}^{(0)}}{dy_T^2} = \left(c_{iT}^{(0)} \right)^\nu - y_T, \quad (S48a)$$

$$\frac{dc_{iT}^{(0)}}{dy_T} = 0 \quad \text{at } y_T = 0, \quad (S48b)$$

$$c_{iT}^{(0)} \rightarrow y_T^{1/\nu} \quad \text{as } y_T \rightarrow \infty. \quad (S48c)$$

As opposed to all the cases outlined above, this problem is nonlinear and does not, in general, have an exact solution. In the particular case of $\nu = 2$, the problem can be mapped to the so-called first Painlevé transcendent^{S1} after a change of variables. This problem has been shown to lack exact solutions in terms of elementary functions so, in order to find a local expansion of its solution, we pose a Taylor series

$$c_{iT}^{(0)} = \alpha + \beta y_T^2 + O(y_T^3), \quad (S49)$$

introduce it in (S48), and obtain $\beta = \alpha^\nu/2$, and where the parameter $\alpha = c_{iT}(0)$ must be calculated by numerically solving (S48).

In summary, the solutions near the bottom and top walls can then be expressed as

$$c_{iB} = 1 - \frac{Da_i^{-1/2}}{\nu} \left[y_B + \frac{e^{-\sqrt{\nu} y_B}}{\nu^{1/2}} \right] + O(Da_i^{-1}), \quad (S50a)$$

$$c_{iT} = \alpha + \frac{\alpha^\nu}{2} y_T^2 + O(y_T^3). \quad (S50b)$$

Changing coordinates to $y_+ = Da_i^{-1/2} y_B$ and $y_- = Da_i^{-\frac{\nu}{3\nu-1}} y_T$ and rescaling, the expansions of the solution

near the walls can be obtained as

$$c_{iB} \approx \left[1 - \frac{Da_i^{-1/2}}{\nu^{3/2}} \right] - Da_i^{-1/2} \frac{y_+^2}{2\nu^{1/2}} \quad \text{at the source,} \quad (\text{S51a})$$

$$c_{iT} \approx Da_i^{-\frac{1}{3\nu-1}} \alpha + Da_i^{\frac{2\nu-1}{3\nu-1}} \frac{\alpha^\nu}{2} y_-^2 \quad \text{at the sink,} \quad (\text{S51b})$$

which coincide with Equations (42) from the main text.

Calibration of particle fluorescence intensity

In order to corroborate that the measured fluorescence intensity is proportional to the particle concentration, we run calibration tests in which particle suspensions at different volume fractions are driven through the same experimental setup, but without the injection of CO_2 or N_2 gases. This causes the particle distribution to remain homogeneous with the known volume fraction introduced through the inlet. Plots of the fluorescent signal as a function of the volume fraction are presented in Figure S1.

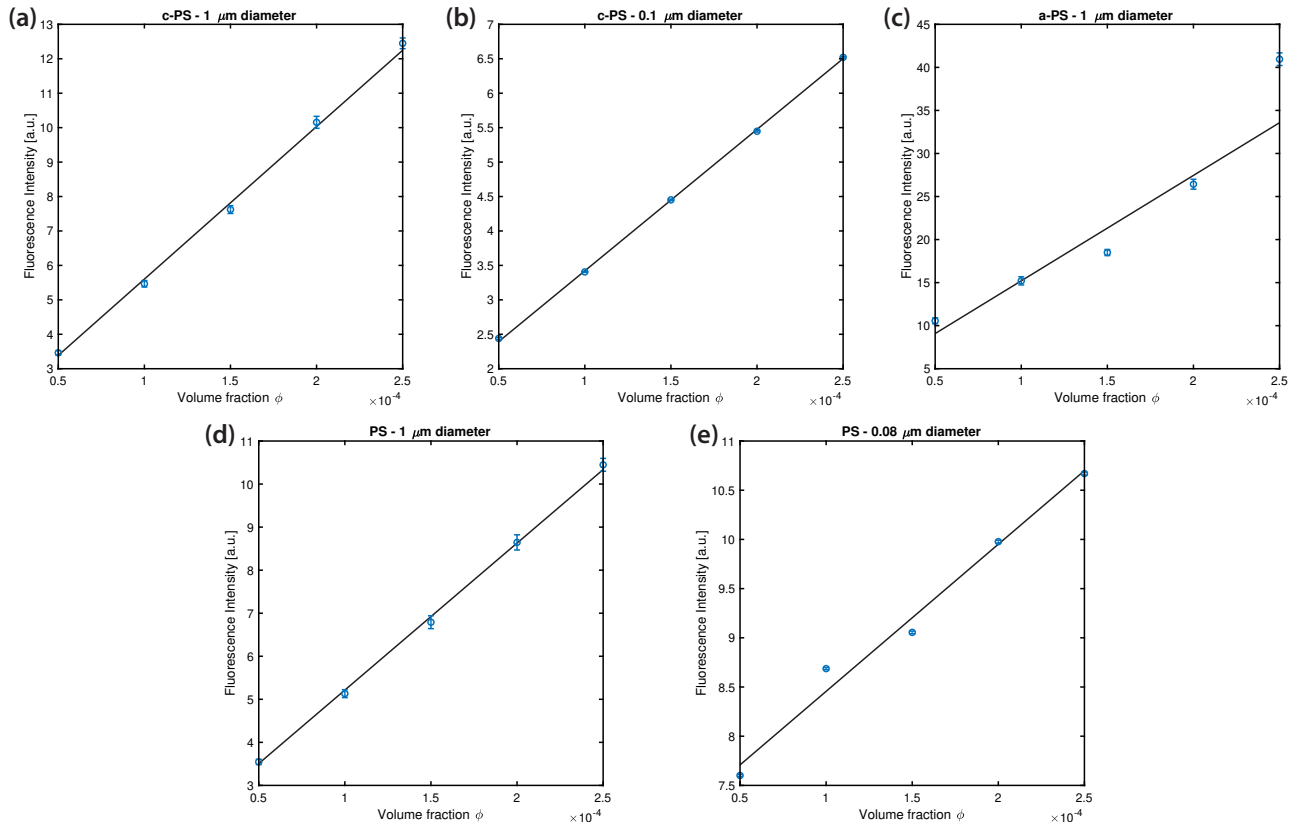


Figure S1: Fluorescence calibration tests for five particle types and sizes. The error bars indicate the standard deviation resulting from averaging the fluorescence signal in time, X , and Y for each calibration test. The black line corresponds to a linear least-squares fit weighted by the standard deviations.

References

(S1) Bender, C. M.; Orszag, S. A. *Advanced mathematical methods for scientists and engineers I: Asymptotic methods and perturbation theory*; Springer, New York, NY, 1999.

TOC Graphic

Some journals require a graphical entry for the Table of Contents. This should be laid out “print ready” so that the sizing of the text is correct.

Inside the `tocentry` environment, the font used is Helvetica 8 pt, as required by *Journal of the American Chemical Society*.

The surrounding frame is 9cm by 3.5cm, which is the maximum permitted for *Journal of the American Chemical Society* graphical table of content entries. The box will not resize if the content is too big: instead it will overflow the edge of the box.

This box and the associated title will always be printed on a separate page at the end of the document.